FE model of three-dimensional steel beam-to-column bolted extended end-plate joint

Concepción Díaz[1], Mariano Victoria[1], Osvaldo M. Querin[2], and Pascual Martí[1]

[1]Department of Structures and Construction. Technical University of Cartagena

Campus Muralla del Mar. C/Doctor Fleming, s/n. 30202 Cartagena, Spain

E-mail: conchi.diaz@upct.es; mariano.victoria@upct.es; pascual.marti@upct.es

Web: http://www.upct.es/goe

[2]School of Mechanical Engineering. University of Leeds

Leeds LS2 9JT, United Kingdom

E-mail: O.M.Querin@leeds.ac.uk

Web: http://www.mech-eng.leeds.ac.uk/menomq/

Abstract:

The rotational behaviour of three-dimensional steel end-plate connections can be studied using the finite element method for the following four reasons: 1) such models are inexpensive and robust; 2) they allow the understanding of local effects; 3) they can be used to generate extensive parametric studies; 4) current version of the component method lacks the appropriate components to predict the behaviour of minor-axis and three-dimensional joints. This work presents a full ANSYS finite element parametric model of a three-dimensional steel beam-to-column bolted extended end-plate joint in both axes for use to obtain their behaviour. The model allows to study four joint configurations (internal, external, corner, and plane) and includes: contact and sliding between different elements; bolt-pretension, and geometric and material non-linearity.

This model was calibrated and validated with experimental results found in the literature. The results from the finite element analysis were verified by comparing the obtained moment-rotation curve of the joint. Three parametric studies are presented to show the versatility of the FE model. The results were compared with those obtained with the model proposed by Eurocode 3. The developed ANSYS FE model can be downloaded for free as a single ZIP compressed file from the Technical University of Cartagena (UPCT): http://www.upct.es/goe/publicaciones/FEM_3D_EEP.zip.

Keyword:

finite element model; three-dimensional steel beam-to-column joint; bolted end-plate connection; moment-rotation curve; non-linear analysis

1. INTRODUCTION

Steel frames were traditionally designed assuming that beam-to-column joints are ideally pinned or fully rigid. The use of the ideally pinned condition implies that no moment can be transmitted between the beam and the column; this means that the connections have no rotational stiffness and cannot transmit moments although they do transmit axial and shear forces to the attached members. On the other hand, fully rigid joints have rotational compatibility and therefore transmit all form of loads between beam and column. An important aspect of the analysis of these joints is that their behaviour is decoupled from the analysis of the structure. Although this simplifies the analysis and structural design processes; it comes at the expense of not being able to obtain a detailed understanding of the behaviour of the joint. In reality, joints have finite stiffness and are therefore semi-rigid.

There are several models which can be used to determine the mechanical behaviour of joints, these are: analytical, empirical, experimental, informational, mechanical and numerical. The most popular of these is the mechanical model, which has several variances, the most popular being the component method (EN 1993-1-8:2005, 2005) of Eurocode 3 (EC3).

The component method is a hybrid analytical-mechanical method. It consists of modelling a joint as an assembly of extensional springs (components) and rigid links, where each spring represents a specific part of a joint with its own strength and rigidity, dependent on the type of loading. The behaviour of the joint is obtained by knowing the mechanical and geometrical properties of each component of the joint. It produces good results when the joint is acting primarily in bending with minimal axial loading. This method is an excellent and versatile analysis tool because of the different components available, where these individual components can be assembled in different ways in order to analyse a wide variety of joints.

The current version of the component method lacks the appropriate components to predict the behaviour of minor-axis joints (the beam is connected to the web of the column, so it is bent around its minor-axis) and the three-dimensional (3D) behaviour of these joints. Components in 3D joints have been less studied but several researchers have performed studies and approaches in the case of this type of joints (Cabrero and Bayo, 2007a; Loureiro *et al*., 2012; Loureiro *et al*., 2013a; Loureiro *et al*., 2013b; Jordão *et al*., 2013; Bayo *et al.*, 2015).

Cabrero and Bayo (2007a) presented a new component for laterally supported plates in bending and it was applied to minor-axis joints. Loureiro *et al*. (2012) focused on the study of a type of 3D joint that consists of extended end-plates for both major and minor axes, as well as to evaluate the interaction between both axes. Loureiro *et al*. (2013a) focused on the stiffness of the E-stub component that appears in 3D joints with additional-plates welded to the column flanges. Loureiro *et al*. (2013b) presented a new analytical formulation for the E-stub strength calculation in 3D steel joints with additional-plates welded to the weak axis. This component is formed by the additional-plates and the column web in tension and the column flanges in bending and is not covered by the formulation in the EC3.

A crucial joint component is the column web under shear. This component has a well-known and defined behaviour for the case of rectangular panels. When the right and left beams have different depths the shear panel becomes trapezoidal. This case has not been researched as much and is not currently covered in component method.

Jordão *et al*. (2013) proposed a modified Atamaz-Jaspart model to capture the distinctive features of double-sided welded joints with beams of unequal depths. Bayo *et al*. (2015) investigated the shear behaviour of stiffened trapezoidal shear panels appearing in joints with unequal beam depths and a mechanical model of rigid bars and springs was proposed to capture the kinematics and internal forces acting on the joint.

Normally the mechanical characteristics of the components are obtained from experimental tests using specimens similar to the component to be characterized or using complete full-scale joints. Today, numerical models based on the Finite Element (FE) Method (FEM) offer a reliable alternative to large-scale laboratory testing and can be used to determine the mechanical behaviour of joints. These models started to be used for several reasons: 1) high cost associated with experimental tests; 2) as a means of overcoming the lack of experimental results; 3) to understand important local effects which can be difficult to measure experimentally with sufficient accuracy, e.g. prying and contact forces between the bolt and the connection components; 4) to generate extensive parametric studies; and 5) to determine the rotational behaviour of a joint.

The first study into joint behaviour using FEM (Bose *et al*., 1972) related to welded beam-to-column joints and included: plasticity, strain hardening and buckling. Sherbourne and Bahaari (1996) developed a model to investigate the behaviour of steel bolted end-plate connections. Bursi and Jaspart (1997a) modelled T-stub connections and isolated extended end-plate connections (Bursi and Jaspart, 1997b; 1998). Bahaari and Sherbourne (2000) developed a detailed 3D model to study 8-bolt unstiffened extended end-plate connections. Tagawa and Gurel (2005) used FE simulations to examine the strength of steel beam-to-column joints stiffened with bolted channels. Maggi *et al*. (2005) carried out parametric analyses on the behaviour of bolted extended end-plate connections using 3D models. Dai *et al*. (2010) made a simulation study of 10 fire tests on restrained steel beam-column assemblies using five different types of joints: fin plate, flexible end-plate, flush end-plate, web cleat and extended end-plate. Augusto *et al*. (2014) presented the development of FE models in ABAQUS with the aim of determining the mechanical properties of steel beam-to-column joint components, which is an essential requirement for the development of a component-based method to use in seismic design of steel frames. Augusto *et al*. (2016) developed a FE model capable of representing the behaviour of extended end-plate joints classified as partial-strength

according to EC3. The model considers non-linear material and geometrical behaviour, non-linear contacts, re-contacts and slip.

Díaz *et al*. (2011) presented a full 3D ANSYS finite element model of steel beam-to-column bolted extended end-plate major-axis joints for use to obtain their behaviour. The model includes: contact and sliding between different elements; bolt pre-tension; and geometric and material non-linearity.

Plane or bi-dimensional (2D) joints subjected to in-plane loading constitute the majority of analysed configurations. However, the literature on 3D joints (with joints in both axes) subjected to out-of-plane loading has a relatively few publications.

Lourerio *et al*. (2012) presented an experimental and numerical analysis of 3D semi-rigid steel joints under non-proportional loading in order to obtain the rotational behaviour (moment-rotation curve) of different 3D configurations, as well as evaluating the interaction between both axes. Loureiro *et al*. (2013a) focused on the stiffness of the E-stub component. Numerical models were calibrated on the basis of the results of six experimental tests with different geometries where column size and bolts distances were taken into account. Gil and Bayo (2008) adjusted, compared and validated several FE models. These models were used to compare the performance of the conventional joints with the proposed alternative design for internal and external semi-rigid composite joints. Dabaon *et al*. (2009) made an experimental investigation to study the behaviour of steel and composite semi-rigid joints. A 3D FE model is proposed using ANSYS software for the analytical investigation. Gil *et al*. (2013) proposed and tested a new design for 3D semi-rigid composite joint in order to improve the behaviour and obtain the benefits of semi-rigidity when the major and minor axes are included. Simultaneously, FE modelling and analysis were carried out and calibrated against the experimental results. These models were performed with the aim of finding tools and ways to characterize and analyse the proposed joint design.

A comprehensive review of the literature about the features of the numerical models of bolted joints provides the following three observations:

1. End-plate joints are the most studied;
2. The majority of the models (Díaz *et al*., 2011) include: bolt contact, pre-tensioning, geometric and material non-linearity;
3. There are few references available on numerical models which take into account 3D out-of-plane behaviour with joints in both axes.

The aim of this work was to develop a full 3D ANSYS (ANSYS, 2016) FE parametric model with joints in both axes to study: 1) the behaviour of 3D steel beam-to-column bolted extended end- plate joints subjected to 3D loading (load in both axes) for three joint configurations: internal, external, and corner; 2) the interaction between both axes for 3D loading; 3) the influence of the minor-axis beams on the major-axis initial stiffness for three joint configurations: external, corner, and plane; 4) the effect of different end- and additional-plate types on the initial rotational stiffness and the design moment resistance. This model includes: contact and sliding between different elements; bolt pre-tension; geometric and material nonlinearity. The results from the FE Analysis (FEA) are calibrated and validated by comparing the obtained moment-rotation curve with those from experimental results found in the literature. The procedure for determining the moment-rotation curve using FEA is also given, together with a brief explanation of how the design moment resistance and the initial rotational stiffness of the joint are obtained.

2. BEAM-TO-COLUMN END-PLATE CONNECTIONS

End-plate connections have become more popular in steel building construction due to their economy, simplicity of fabrication, and good structural performance (Bursi and Jaspart, 1998; Bahaari and Shebourne, 2000; Gan *et al.* 2017). End-plate connections can be classified into four typologies (Fig. 1): header, flush, extended and double

extended end-plate connections. If the length of the end-plate is less than the depth of the beam, it is called header end-plate (Fig. 1a); if it is approximately the same height as the beam depth it is called flush end-plate (Fig. 1b); if its height is significantly larger than the beam height using the space: 1) above (or below); 2) above and below the beam for additional rows of bolts, it is called extended (Fig. 1c) or double extended (Fig. 1d) end-plate, respectively.

In this work, the 3D FE model is calibrated and validated using an internal joint configuration. This 3D joint was proposed by Cabrero and Bayo (2007a; 2007b) and it is shown in Fig. 2a. It consists of extended end-plate joints for both major (M) and minor (n) axes with symmetrical loading and boundary conditions. The minor-axis joint is bolted to a plate welded to the column flanges (additional-plate). The end- and additional-plate consist of two partial plates in both tension and compression regions. The external (Fig. 2b), corner (Fig. 2c), and plane joint (Fig. 2d) configurations represent an extension of the FE model and these are analysed parametrically in Section 6.

There are two main advantages of using this type of 3D joint which is characterized by the additional-plate, these are: 1) both major and minor axis joints do not interfere, making the assembly easier; 2) the additional-plate contributes to the stiffness and resistance of the column web in tension, compression, and shear regions.

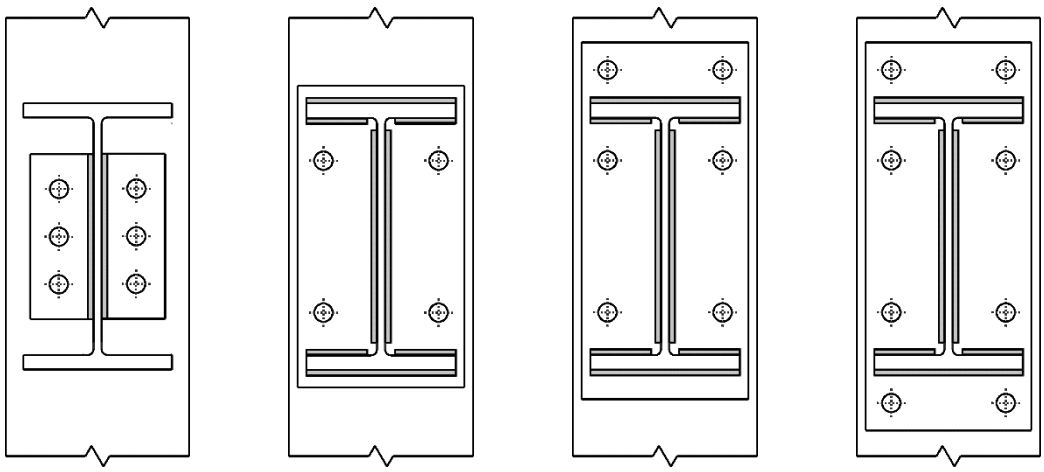

(a) (b) (c) (d)

Figure 1. Beam-to-column end-plate connections: a) header; b) flush; c) extended; d) double extended.

The FE model used to represent this joint uses 3D elements for all components (column, beams, end-plates, additional-plate, bolts head, shanks and nuts, and welds). In the analysis, contact, sliding between components, bolt pre-tensioning, and geometric and material non-linearity were considered.

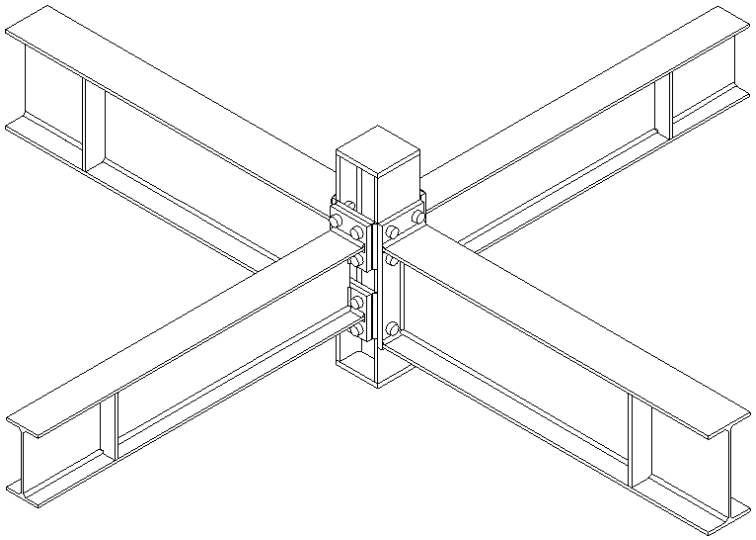

(a)

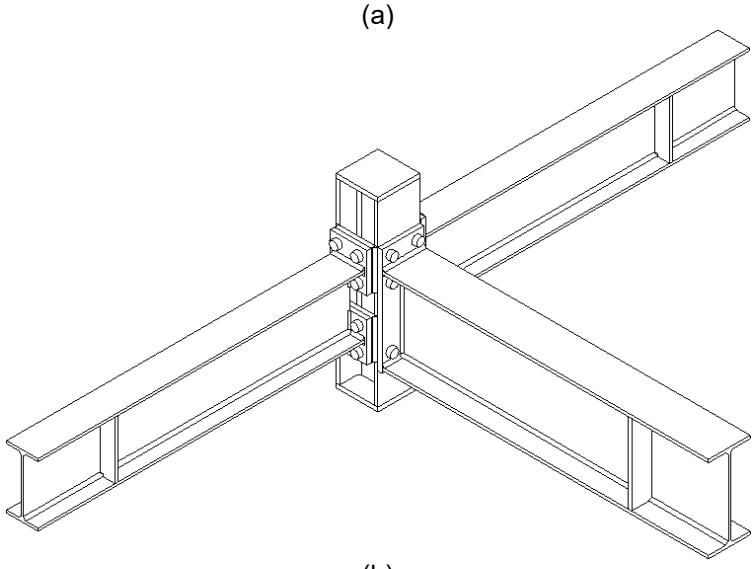

(b)

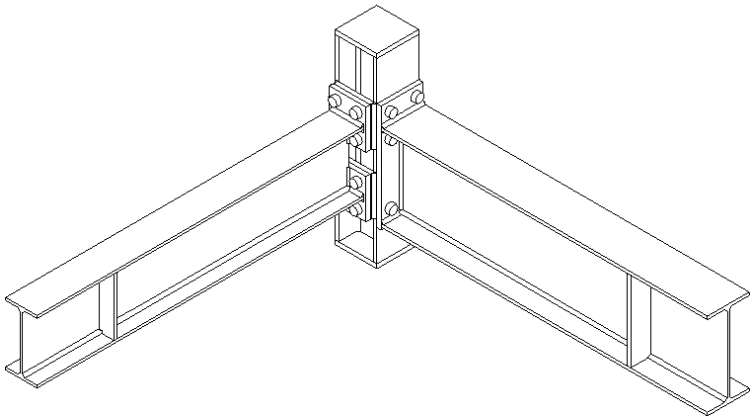

(c)

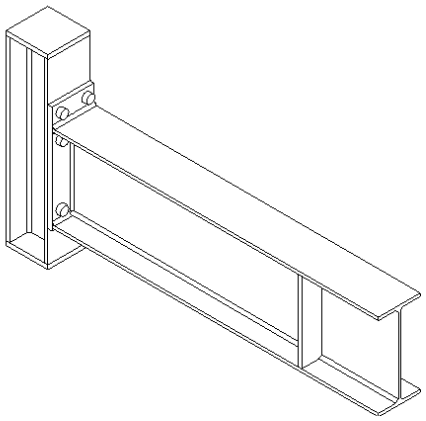

(d)

Figure 2. 3D beam-to-column bolted extended end-plate: (a) internal, (b) external, (c) corner, (d) plane joints.

3. THE FINITE ELEMENT MODEL

The FE program ANSYS was used to develop and analyse the numerical model, which was based on the experimental model made by Cabrero and Bayo (2007b).

3.1. Definition of the internal joint configuration

The parameters that define the internal joint; which consists of the beams, column, additional-plates, extended end-plates, and bolts; are arranged into two groups: 1) dimensions, Table 1 and Fig. 3; 2) material properties, Table 2 and Fig. 4.

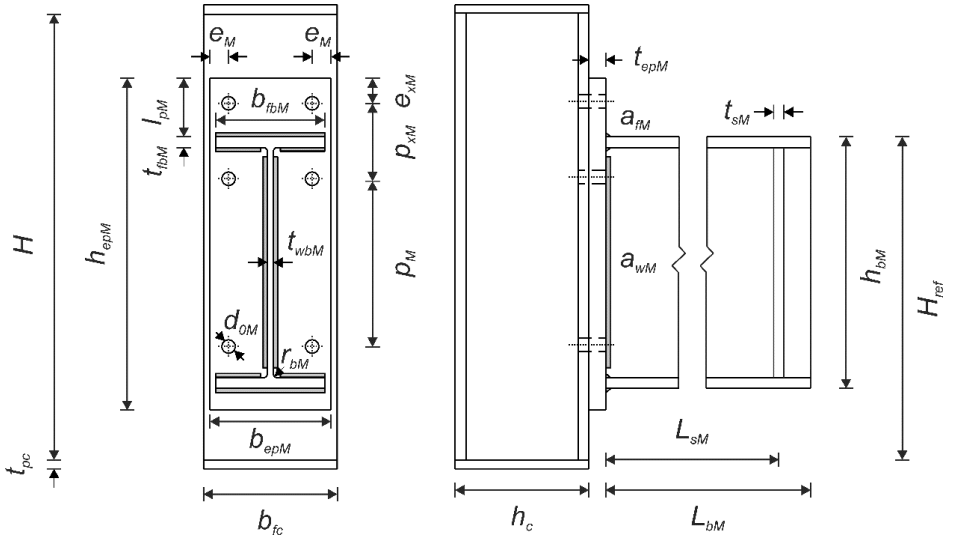
e_M
e_M
b_{fbM}
l_{pM}
t_{fbM}
e_{xM}
p_{xM}
p_M
t_{wbM}
d_{0M}
r_{bM}
H
h_{epM}
t_{pc}
b_{epM}
b_{fc}
t_{epM}
a_{fM}
t_{sM}
a_{wM}
h_{bM}
H_{ref}
L_{sM}
h_c
L_{bM}

(a)

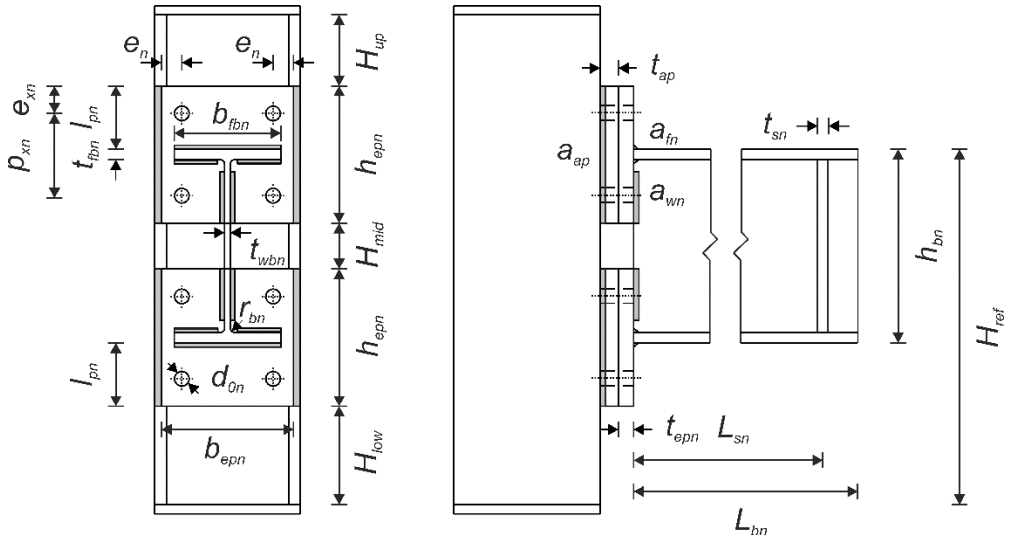
e_n
e_n
H_{up}
e_{xn}
p_{xn}
l_{pn}
b_{fbn}
t_{fbn}
h_{epn}
t_{wbn}
H_{mid}
r_{bn}
h_{epn}
l_{pn}
d_{0n}
b_{epn}
H_{low}
t_{ap}
a_{ap}
a_{fn}
t_{sn}
a_{wn}
h_{bn}
H_{ref}
t_{epn}
L_{sn}
L_{bn}

(b)

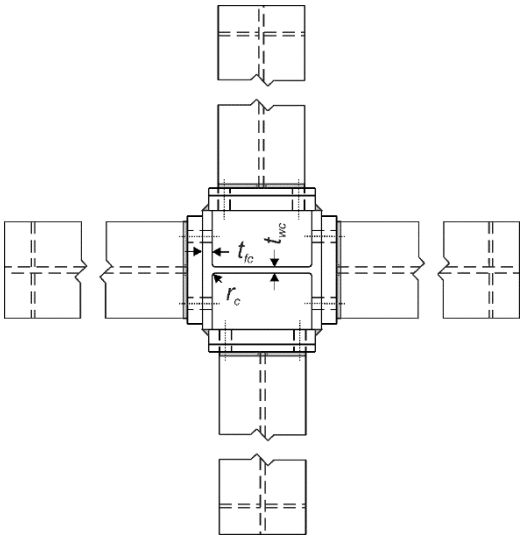
t_{fc}
t_{wc}
r_c

(c)

Figure 3. Dimensions of 3D beam-to-column extended end-plate internal joint: (a) major-axis; (b) minor-axis; (c) complete views.

1. Dimensions:

   Major-axis connection (Fig. 3a)

   a. Beam: flange width (b_{fbM}), height (h_{bM}), length (L_{bM}), root radius (r_{bM}), flange thickness (t_{fbM}), and web thickness (t_{wbM}).

   b. Bolt: tensile stress area (A_{sM}), hole clearance (d_{0M}), nominal diameter (d_{bM}), head diameter (d_{hbM}), nut diameter (d_{nbM}), edge distance (e_M), distance from the upper tension row to the top of the end-plate (e_{xM}), distance between the lower tension row and the compression row (p_M), distance between the tension rows (p_{xM}), head thickness (t_{hbM}), nut thickness (t_{nbM}).

   c. End-plate: width (b_{epM}), height (h_{epM}), distance of the upper edge below the beam top flange (l_{pM}), and thickness (t_{epM}).

   d. Stiffener: distance from the face of the end-plate to the centre of the stiffener location (L_{sM}), and stiffener thickness (t_{sM}).

   e. Weld throat thicknesses: beam flange and end-plate (a_{fM}), beam web and end-plate (a_{wM}).

   Minor-axis connection (Fig. 3b)

   f. Additional-plate: thickness (t_{ap}).

   g. Beam: flange width (b_{fbn}), height (h_{bn}), distance from the top flange to the column lower edge (H_{ref}), length (L_{bn}), root radius (r_{bn}), flange thickness (t_{fbn}), and web thickness (t_{wbn}).

   h. Bolt: tensile stress area (A_{sn}), hole clearance (d_{0n}), nominal diameter (d_{bn}), head diameter (d_{hbn}), nut diameter (d_{nbn}), edge distance (e_n), distance from the upper tension row to top of the end-plate (e_{xn}), distance between the tension rows (p_{xn}), head thickness (t_{hbn}), nut thickness (t_{nbn}).

i. End-plate: width (b_{epn}), height (h_{epn}), distance of the upper edge below the beam top flange (l_{pn}), and thickness (t_{epn}).

j. Stiffener: distance from the face of the end-plate to the centre of the stiffener location (L_{sn}), and stiffener thickness (t_{sn}).

k. Weld throat thicknesses: column flange and additional-plate (a_{ap}), beam flange and end-plate (a_{fn}), beam web and end-plate (a_{wn}).

Column (Figs. 3a, 3b, and 3c)

l. Column: flange width (b_{fc}), length (H), height (h_c), clearance below the bottom minor-axis end-plate (H_{low}), clearance between the minor-axis end-plates (H_{mid}), clearance above the top minor-axis end-plate (H_{up}), root radius (r_c), flange thickness (t_{fc}), and web thickness (t_{wc}).

m. Plate: thickness (t_{pc}).

2. Material properties:

a. Steel: elasticity modulus (E), Poisson's ratio (ν), specific weight (γ).

Major-axis connection

b. Beam: flange ultimate stress ($f_{u,fbM}$), web ultimate stress ($f_{u,wbM}$), flange yield stress ($f_{y,fbM}$), and web yield stress ($f_{y,wbM}$).

c. Bolt: ultimate stress ($f_{u,bM}$) and yield stress ($f_{y,bM}$).

d. End-plate: ultimate stress ($f_{u,epM}$) and yield stress ($f_{y,epM}$).

e. Stiffener: ultimate stress ($f_{u,sM}$) and yield stress ($f_{y,sM}$).

f. Weld: ultimate stress ($f_{u,wM}$) and yield stress ($f_{y,wM}$).

Minor-axis connection

g. Additional-plate: ultimate stress ($f_{u,apn}$) and yield stress ($f_{y,apn}$).

h. Beam: flange ultimate stress ($f_{u,fbn}$), web ultimate stress ($f_{u,wbn}$), flange yield stress ($f_{y,fbn}$), and web yield stress ($f_{y,wbn}$).

i. Bolt: ultimate stress ($f_{u,bn}$) and yield stress ($f_{y,bn}$).

j. End-plate: ultimate stress ($f_{u,epn}$) and yield stress ($f_{y,epn}$).

k. Stiffener: ultimate stress ($f_{u,sn}$) and yield stress ($f_{y,sn}$).

l. Weld: ultimate stress ($f_{u,wn}$) and yield stress ($f_{y,wn}$).

Column

m. Column: flange ultimate stress ($f_{u,fc}$), web ultimate stress ($f_{u,wc}$), flange yield stress ($f_{y,fc}$), and web yield stress ($f_{y,wc}$).

3.1.1. Dimensions

Table 1 gives the dimensions used for the internal joint. The geometrical dimensions of the profiles for the joint were obtained from the Arcelor group catalogue (ArcelorMittal, 2016) and for the bolts from EN 14399-3:2005 (2005). In order to prevent local effects under the reactions, the thickness of the stiffeners (t_{sM}, t_{sn}) were set to be equal to that of the beam flange thicknesses (t_{fbM}, t_{fbn}) (Díaz, 2010; Díaz *et al*., 2011).

Table 1. Dimensions of the joint (mm and mm^2).

Major-axis												
Beam (IPE 330)		Bolt (TR20)				End-plate		Stiffener		Weld		
b_{fbM}	160.0	A_{sM}	245.0	e_{xM}	30.0	b_{epM}	160.0	L_{sM}	950.0	a_{fM}	6.5	
h_{bM}	330.0	d_{0M}	22.0	p_M	230.0	h_{epM}	410.0	t_{sM}	11.5	a_{wM}	5.0	
L_{bM}	1250.0	d_{bM}	20.0	p_{xM}	90.0	l_{pM}	70.0					
r_{bM}	18.0	d_{hbM}	32.0	t_{hbM}	12.5	t_{epM}	16.0					
t_{fbM}	11.5	d_{nbM}	32.0	t_{nbM}	18.0							
t_{wbM}	7.5	e_M	30.0									
Minor-axis												
Additional-plate		Beam (IPE 240)		Bolt (TR20)				End-plate		Stiffener		Weld
t_{ap}	16.0	b_{fbn}	120.0	A_{sn}	245.0	p_{xn}	90.0	b_{epM}	140.0	L_{sn}	950.0	a_{ap} 9.0
		h_{bn}	240.0	d_{0n}	22.0	t_{hbn}	12.5	h_{epn}	150.0	t_{sn}	9.8	a_{fn} 6.5
		H_{ref}	460.0	d_{bn}	20.0	t_{nbn}	18.0	l_{pn}	70.0			a_{wn} 5.0
		L_{bn}	1250.0	d_{hbn}	32.0			t_{epn}	16.0			

		r_{bn}	15.0	d_{nbn}	32.0
		t_{fbn}	9.8	e_n	30.0
		t_{wbn}	6.2	e_{xn}	30.0
Column					
Column (HE160B)				Plate	
b_{fc}	160.0	H_{up}	150.0	t_{pc}	16.0
H	680.0	r_c	15.0		
h_c	160.0	t_{fc}	13.0		
H_{low}	150.0	t_{wc}	8.0		
H_{mid}	80.0				

where:

$$H_{mid} = h_{bn} - 2\left(h_{epn} - l_{pn}\right); \quad H_{ref} = H - H_{up} - l_{pn}$$

3.1.2. Material properties

The standard mechanical properties for the joint which were obtained from EN 1993-1-1:2005 (2005) and EN 1993-1-8:2005 (2005) are given in Table 2. The material for the column plates, located at the top and bottom of the column, was assumed to behave linearly with an elasticity modulus equal to $100 \times E$. These plates were introduced into the model to prevent the localised effect of the loading condition from being transmitted to the column.

The plasticity behaviour in the joint was represented by the isotropic work hardening assumption and the von Mises yield criterion.

Table 2. Material properties used for the joint (nominal values in MPa and kN/m^3).

Material (steel)					
E	210000	ν	0.3	γ	78.5

Major-axis (S275)												
Beam				Bolt (grade 8.8)		End-plate		Stiffener		Weld		
$f_{u,fbM}$	430	$f_{y,fbM}$	275	$f_{u,bM}$	800	$f_{u,epM}$	430	$f_{u,sM}$	430	$f_{u,wM}$	430	
$f_{u,wbM}$	430	$f_{y,wbM}$	275	$f_{y,bM}$	640	$f_{y,epM}$	275	$f_{y,sM}$	275	$f_{y,wM}$	275	
Minor-axis (S275)												
Additional-plate		Beam				Bolt (grade 8.8)		End-plate		Stiffener		Weld
$f_{u,apn}$	430	$f_{u,fbn}$	430	$f_{y,fbn}$	275	$f_{u,bn}$	800	$f_{u,epn}$	430	$f_{u,sn}$	430	$f_{u,wn}$ 430
$f_{y,apn}$	275	$f_{u,wbn}$	430	$f_{y,wbn}$	275	$f_{y,bn}$	640	$f_{y,epn}$	275	$f_{y,sn}$	275	$f_{y,wn}$ 275
Column (S275)												
$f_{u,fc}$	430	$f_{u,wc}$		430	$f_{y,fc}$	275		$f_{y,wc}$		275		

The material behaviour used for the joint (beams, column and connections) was represented by the tri-linear stress-strain curve of Fig. 4, where the elastic moduli for the three segments are:

1. Region (a): elasticity modulus (E), (EN 1993-1-1:2005, Section 3.2.6, 2005).
2. Region (b): $E_{h_1} = \left(f_u - f_y\right) \big/ \left(\varepsilon_u - \varepsilon_y\right)$, with $\varepsilon_u = 15\varepsilon_y$, where ε_u is the ultimate strain and ε_y the yield strain, with $\varepsilon_y = f_y \big/ E$, (EN 1993-1-1:2005, Section 3.2.2, 2005).
3. Region (c): $E_{h_2} = 0$, with $\varepsilon_r = 10\varepsilon_u$.

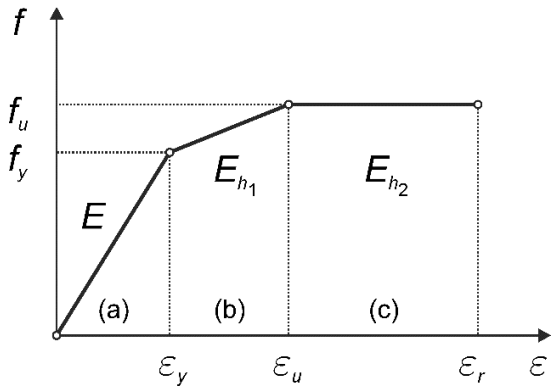

Figure 4. Material stress-strain curve.

3.2. Generation of the FE model

In order to represent the joint with FE, the following simplifications were assumed:

1. The bolt shank was modelled by a cylinder with a diameter of 17.66 mm and calculated from the bolt tensile stress area (A_s), Table 1.
2. The root radii were represented by a right angle isosceles triangle with an area equivalent to that enclosed by the radius.
3. Washers were not included in order to reduce the number of contact regions.
4. The welds were modelled by a right angle isosceles triangle with an area equivalent to that enclosed by the weld.

Symmetry conditions on the planes perpendicular to the major and minor axes were used to reduce the computational cost. The geometry was subdivided with regular volumes in order to generate both a mapped mesh and for all the contact surfaces to have matching coincident areas, Fig. 5.

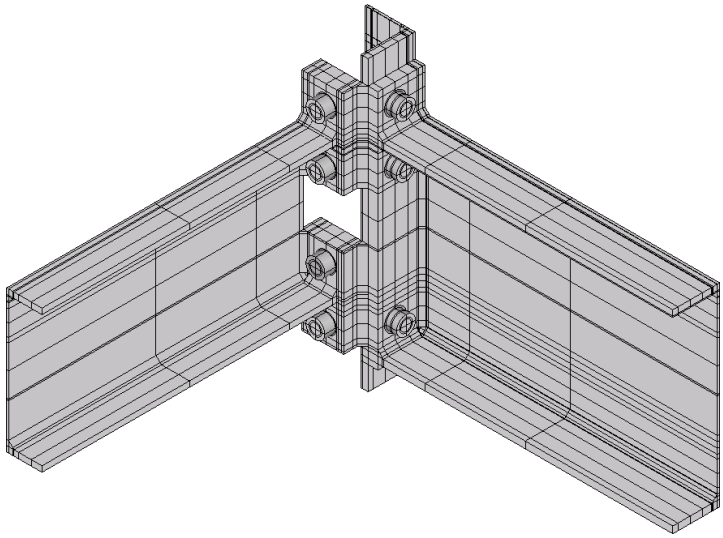

Figure 5. Detail of isometric view of the geometry of the internal joint.

3.2.1. Meshing

The FE used was the 8-node brick which used uniform reduced integration with hourglass control and suppressed extra displacement shapes (SOLID45). The vast majority of the elements produced by the meshing process were of this type, with very

few degenerated elements such as the wedge generated in the bolt heads, root radii and welds.

The contact elements CONTA173 and TARGE170 were used on all contact surfaces of the joint: end-plate and bolt nut, column flange and bolt head/end-plate, bolt shank and end-plate/column flange hole, end-plate and beam, additional-plate and bolt head/end-plate, bolt shank and end- and additional-plate hole. Bolt preloading was modelled using the PRETS179 element. A full review of these elements can be found in ANSYS (2016).

The generation of the FE mesh was controlled by two parameters related to the maximum length of a FE: 1) the length of the elements in the region near the connection $\left(l_{en}\right)$; 2) the length of the elements in the region far from the connection $\left(l_{ef}\right)$. The range of values used is given in Table 3. The region near the connection is defined by the rectangle of height $\left(H_{low}+H_{mid}+2h_{epn}+h_c/4\right)$, and width $\left(h_c+t_{epM}\right)$ for the major-axis and $\left(h_c/2+t_{epn}+t_{ap}+b_{fc}/2\right)$ for the minor-axis, Fig. 6.

Table 3. Mesh characteristics of the FE models.

Mesh	$l_{en}\left(\text{mm}\right)$	$l_{ef}\left(\text{mm}\right)$	Elements	Nodes	Degrees of freedom
Coarse	10	35	23176	28054	78908
Fine	7	25	46625	55602	157104
Extra-fine	5	20	88340	104624	298441

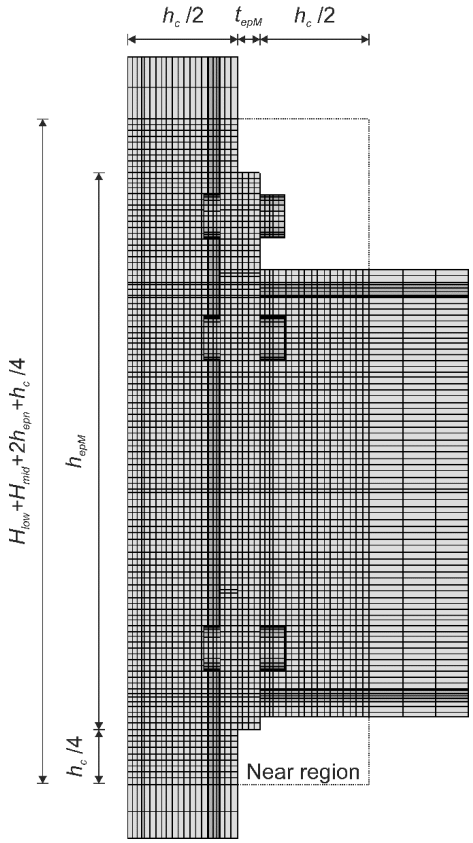
$h_c/2$
t_{epM}
$h_c/2$
$H_{low}+H_{mid}+2h_{epn}+h_c/4$
h_{epM}
$h_c/4$
Near region

(a)

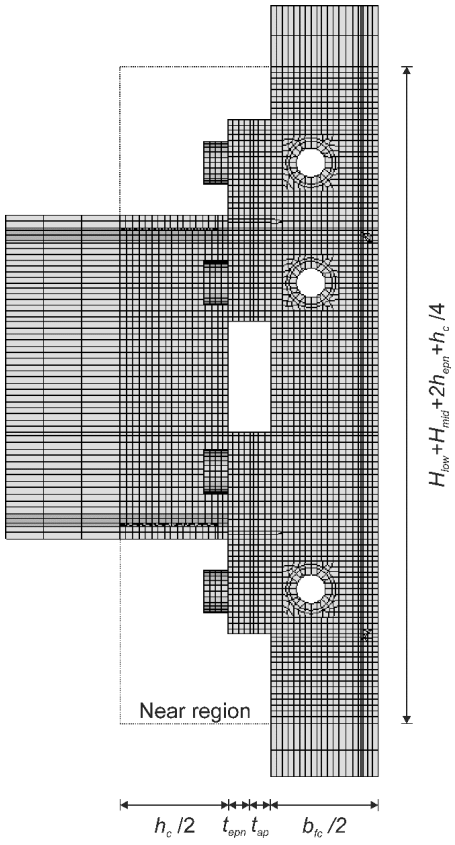
$H_{low}+H_{mid}+2h_{epn}+h_c/4$
Near region
$h_c/2$
t_{epn}
t_{ap}
$b_{fc}/2$

(b)

Figure 6. Detail of the mesh model of the internal joint: (a) major-axis; (b) minor-axis views.

3.2.2. Loading and supporting conditions

Two different loading and supporting condition types were used. In both types the self-weight of model was also included in the analysis:

Type I (Figs. 7a and 7b): it was used to calibrate and validate the FE model (Section 5). These conditions replicate the loading procedure followed by Cabrero and Bayo (2007b). The beams were pinned supported at a distance of L_{sM} and L_{sn} to the face of the end-plates. The supports were located on the top face of the beams. Since the joint is symmetrical about a perpendicular plane to major- and minor-axes, symmetry conditions were applied, not allowing any displacements perpendicular to the symmetry planes. The load was applied to the lower plate of the column and was modelled as an upward pressure boundary condition (Q).

Type II (Figs. 7c and 7d): it was used to analyse parametrically the FE model (Section 6) in order to study the effect on joint behaviour of 3D loading, minor-axis beams, and entire end- and additional-plates. The column was fixed supported at both ends and P_M and P_n loads were applied at the free end of each beam.

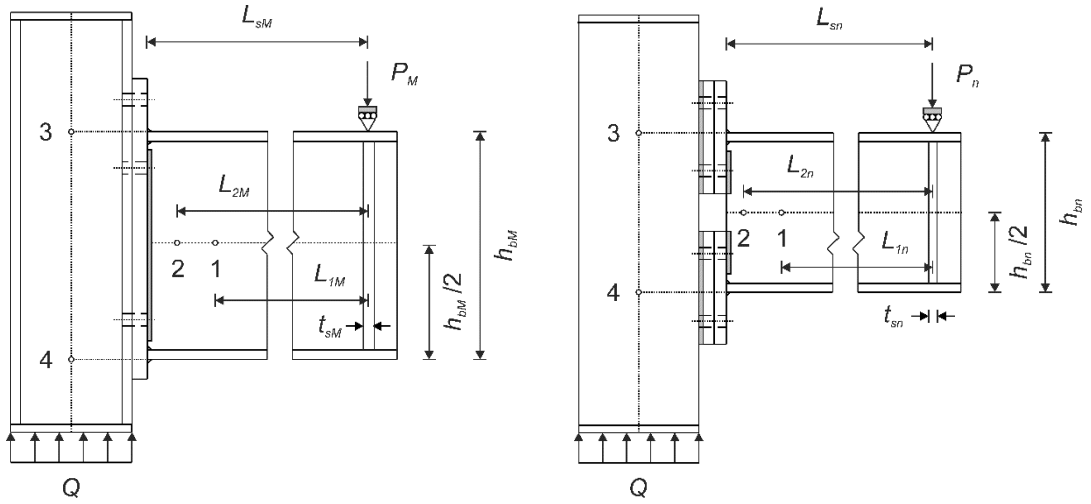

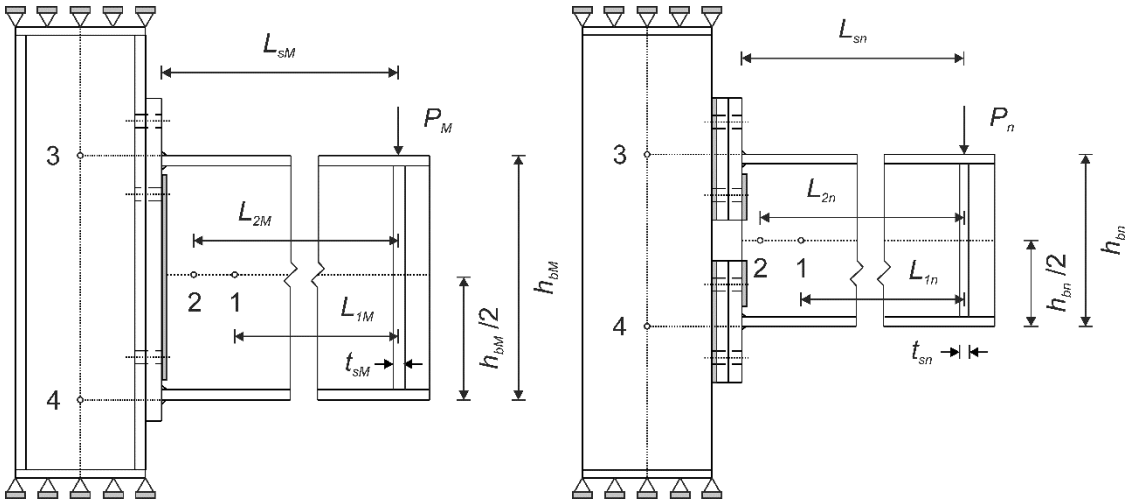

(c) (d)

Figure 7. Loading and supporting conditions: (a), (b) type I; (c), (d) type II. Reference points used to calculate the rotational deformation of the joint: (a), (c) major-axis; (b), (d) minor-axis views.

3.2.3. Loading procedure

The FE model is used to calculate the moment-rotation curve, from which the initial rotational stiffness $S_{j,ini,FEM}$ and design moment resistance of the joint $M_{j,Rd,FEM}$ are determined. This was done by the following three stage loading scheme, Fig. 8:

1. To simulate the hand-tightened to apply 30% of the pretension force $\left(F_p\right)$, given by Eq. (1), required in case of preloaded bolts (EN 1993-1-8:2005, 2005; Cabrero and Bayo, 2007b; Loureiro *et al*., 2012).

$$F_p = 0.7 f_{u,b} \times A_s / \gamma_{M7} \tag{1}$$

Where $f_{u,b}$ is the ultimate tensile strength, A_s is the tensile stress area of the bolt, γ_{M7} is a partial safety factor about preload of high strength bolts (recommended value is $\gamma_{M7} = 1.1$).

2. Apply the load *Q* incrementally until the applied moment is equal to the ultimate flexural resistance of joint $\left(M_{j,\mathrm{u}}\right)$ or until the solution fails to converge (*A*-*B* of Fig. 8).

3. The two first points of the nonlinear analysis were used to calculate the initial stiffness $\left(S_{j,ini,FEM}\right)$. Alternatively, a linear re-analysis of the model (*A*-*C* of Fig. 8) can be used in order to determine this value.

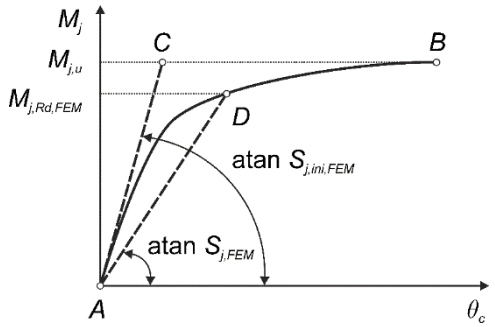

Figure 8. Loading process: pre-loading (*A*), loading (*A*-*B*), linear re-analysis (*A*-*C*).

3.3 Analysis

Material and geometric non-linear analysis was carried out to predict the moment-rotation curve of the joint without considering geometrical imperfections. The settings in ANSYS (2016) included: the allowable elastic slip factor (*SLTO*) value of 0.01 (Section 5.2); automatic stepping; Newton-Raphson equation solver; contact algorithm penalty function; a convergence criterion of 0.5% for force or moment checking; the friction coefficient $\left(\mu\right)$ value of 0.5 (Díaz *et al*., 2011); and the normal penalty stiffness factor (*FKN*) value of 1.0 (Section 5.2).

4. THE MOMENT-ROTATION CURVE

Beam-to-column joint behaviour may be represented by a moment-rotation curve $\left(M_j - \phi_j\right)$. This curve describes the relationship between the bending moment $\left(M_j\right)$ applied to a joint and the corresponding rotation $\left(\phi_j\right)$ between the connected members. In this work, this curve was used to calibrate and validate (Section 5) the FE model by

comparing the obtained moment-rotation curve with those from experimental results found in the literature (Cabrero and Bayo, 2007b).

4.1. Bending moment

The bending moment M_j, Eq. (2), acting on the joint corresponds to the applied force P (P_n and P_M for the minor- and major-axes respectively, Fig. 7) multiplied by the distance between the force application point and the face of the end-plate, L_s (L_{sn} and L_{sM} for the minor- and major-axis respectively, Fig. 7).

$$M_j = P \times L_s \tag{2}$$

4.2. Joint rotation

The rotational deformation of the joint $\left(\phi_j\right)$ is the sum of the shear deformation of the column web panel zone $\left(\gamma\right)$ and of the connection rotational deformation $\left(\theta_c\right)$, given by Eq. (3).

$$\phi_j = \theta_c + \gamma \tag{3}$$

Displacement values in the reference points (1, 2, 3, and 4) of Fig. 7 were used to determine: the rotational deformation of the joint, Eqs. (4), (7), (8) and (9); the shear deformation of the column web panel zone, Eqs. (5) and (9); and the connection rotational deformation, Eqs. (6), (7), (8), and (9).

$$\phi_j = \text{atan}\left(\frac{\left(V_2 - V_{el,b2} - V_{el,bv2}\right) - \left(V_1 - V_{el,b1} - V_{el,bv1}\right)}{L_2 - L_1}\right) - \theta_{el,c} \tag{4}$$

$$\gamma = \text{atan}\left(\frac{U_4 - U_3}{d_{34}}\right) - \theta_{el,c} \tag{5}$$

$$\theta_c = \text{atan}\left(\frac{\left(V_2 - V_{el,b2} - V_{el,bv2}\right) - \left(V_1 - V_{el,b1} - V_{el,bv1}\right)}{L_2 - L_1}\right) - \text{atan}\left(\frac{U_4 - U_3}{d_{34}}\right) \tag{6}$$

where:

V_1, V_2 are the vertical displacements at points 1 and 2

$V_{el,b1}$, $V_{el,b2}$ are the beam elastic vertical displacements at points 1 and 2, given by Eq. (7)

$V_{el,bv1}$, $V_{el,bv2}$ are the beam shear elastic vertical displacements at points 1 and 2, given by Eq. (8)

L_1, L_2 are the distances between points 1 and 2 at centre of the stiffener, given by Eqs. (10) and (11)

$\theta_{el,c}$ is the theoretical column elastic rotation, given by Eq. (9)

$$V_{el,bi} = \frac{P \times L_i \left(3L_s^2 - L_i^2\right)}{6E \times I_b} \tag{7}$$

$$V_{el,bv} = \frac{P \times L_i}{G \times A_{vb}} \tag{8}$$

$$\theta_{el,c} = \frac{M_j \times H}{16E \times I_c} \tag{9}$$

I_c, I_b are the second moment of areas of the column and beam

U_3, U_4 are the horizontal displacements at points 3 and 4

d_{34} is the distance between points 3 and 4, and also the beam height (h_b)

G is the shear modulus $= E/\left(2\left(1+\nu\right)\right)$

A_{vb} is the shear area of the beam

The reference points 1 and 2 (shown in Fig. 7) were located on the longitudinal axis of the beam at a distance of L_1 and L_2 from the centre of the stiffener (Eqs. 10 and 11, units in mm), and 3 and 4 were located on the longitudinal axis of the column at a height fixed by the lower and upper plates of the beam.

$$L_1 = L_s - 500 \tag{10}$$

$$L_2 = L_s - 250 \tag{11}$$

4.3. Design moment resistant of the joint

The initial rotational stiffness of the joint ($S_{j,ini,FEM}$) calculated in step 3 of Section 3.2.3 and the moment rotation curve calculated in the Section 4.2 are used to calculate the design moment resistance value ($M_{j,Rd,FEM}$), using the following two steps (Eurocode 3, EN 1993-1-8:2005, 2005; Faella *et al*., 2000):

1. Calculate the secant stiffness $\left(S_{j,FEM}\right)$ using Eq. (12).

$$S_{j,FEM} = \frac{1}{3} S_{j,ini,FEM} \tag{12}$$

2. The design moment resistance value ($M_{j,Rd,FEM}$) is obtained by the intersection of the moment rotation curve and a line from the origin with slope $\left(S_{j,FEM}\right)$, point *D* in Fig. 8.

5. CALIBRATION OF THE FE MODEL

To calibrate the FE model, the results were compared with the experimental results of Cabrero and Bayo (2007b) obtained using the A-n test. The dimensions of the joint and material properties are given in Table 1 and Table 2, respectively. Note that the A-n test configuration has only supporting conditions at the minor-axis (2D loading).

The calibration of the FE model consisted in determining these four parameters: the coefficient of friction $\left(\mu\right)$, the element size, the allowable elastic slip factor (*SLTO*) and the normal penalty stiffness factor (*FKN*). Also checked that the failure mode of the FE model matched that of the experiment. The study consisted of two steps:

1. Using the default values from ANSYS (2016) of *FKN* = 1 and *SLTO* = 0.01, determine the friction coefficient value and mesh density via the following two stages:

i. Carry out an exhaustive search with four friction coefficients μ (0.2, 0.3, 0.4, 0.5) and three mesh densities (coarse, fine, and extra-fine, see Table 3) to determine the friction coefficient value that consistently gives the least error in calculating the moment-rotation curve.

ii. Using the friction coefficient values from stage (i) determine the most appropriate mesh density.

2. Using the friction coefficient value and mesh density from step 1, carry out an exhaustive search to determine the values of *FKN* (0.10, 0.25, 0.50, 0.75, and 1.00) and *SLTO* (0.001, 0.010, 0.100, and 1.000).

The FE analysis was carried out in a Dell Precision Tower 5810 with 4 cores and 8 threads Intel Xeon CPU E5-1620 v3 @ 3.5 GHz and 16 GB of RAM. The average computational time analysis of the 3D model was about 20 minutes.

5.1. Moment-rotation curve fitting

To calibrate the FE model, the resulting moment-rotation curve was compared with that obtained experimentally by Cabrero and Bayo (2007b) for the A-n test. Their experimental data was used to generate the sextic polynomial curve of best fit of Eq. (13) with an R-square $\left(R^2\right)$ goodness-of-fit value, Eq. (14), of $R^2 = 0.999$, used in this comparison.

$$p(x) = 28.314x^6 - 3.711x^5 + 0.263x^4 - 0.010x^3 + 0.000x^2 + 0.000x - 6.171 \qquad (13)$$

$$R^2 = 1 - \frac{\sum_{i=1}^{n_p}\left(y_i - \hat{y}_i\right)^2}{\sum_{i=1}^{n_p}\left(y_i - \overline{y}\right)^2} \qquad (14)$$

where y_i is the real value and $\hat{y}_i$ is the predicted value at the *ith* point, $\overline{y}$ is the mean of the point values, and n_p is the number of points. R-square can take on any value between 0 and 1, with a value closer to 1 indicating that a greater proportion of variance is accounted for by the fit.

5.2. Calibration using the moment-rotation curve

A useful means to determine the accuracy of the FE model is the R^2 value, Eq. (14). The larger the value of R^2, the more accurate is the FE model. However, no single rule exits that specifies a minimum R^2 value which guarantees a good fitting FE model. For this reason, it was thought appropriate to only consider FE models with R^2 values greater than 0.94.

The parametric study on the μ for different mesh density (Fig. 9) revealed that: 1) the nearest R^2 value to 1 in the prediction of the moment-rotation curve was obtained using the fine mesh and the friction coefficient $\mu = 0.2$. Note that the fine mesh uses three elements through the thickness of the end-plate which is the recommended minimum number of elements by Bursi and Jaspart (1997a); 2) the extra-fine mesh provided R^2 values slightly lower than those obtained using the fine mesh.

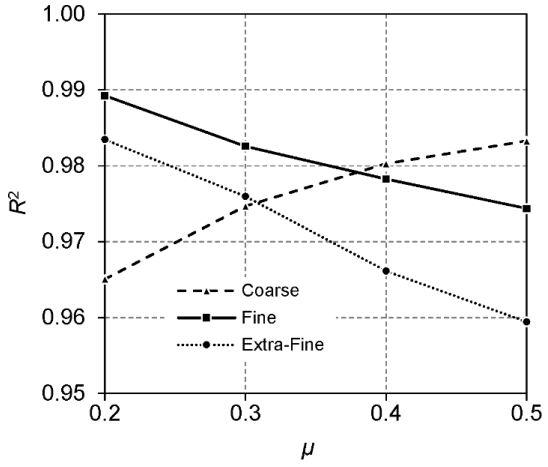

Figure 9. Plot of the variation of R^2 with μ for the different mesh densities.

A comparison of the knee region moment-rotation curves produced from the FE models with μ (0.2, 0.3, 0.4, 0.5) for the different mesh densities with the experimental curve of the test A-n is given in Fig. 10. For clarity, only the moment-rotation curves with μ (0.2 and 0.5) are shown. The comparison demonstrated that: 1) the resulting FE models with extra-fine mesh and μ values over 0.2 were stiffer and more resistant than experimental model; 2) the resulting FE models with coarse mesh for all μ values were softer than experimental model; 3) The best fit of the A-n test curve was obtained using the fine mesh and the friction coefficient $\mu = 0.2$ (Fig. 10), which may explain its highest value of R^2 statistic (Fig. 9).

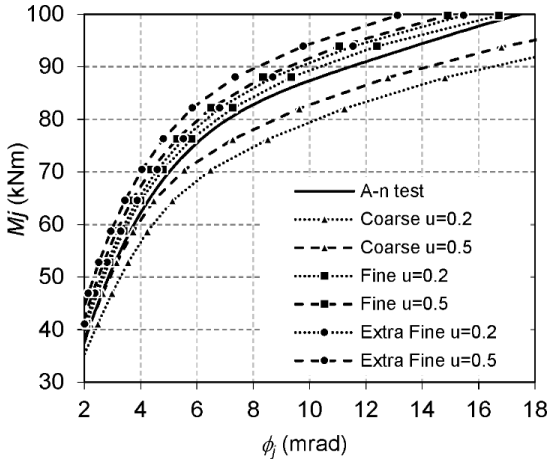

Figure 10. Plot of the knee region moment-rotation curve with μ (0.2 and 0.5) for the different mesh densities.

The parametric study on the contact parameters (Fig. 11) revealed that: 1) the values which gave the highest R^2 were $FKN = 0.1$ and $SLTO = 0.01$; 2) with $FKN = 0.1$ are obtained the higher R^2 values for all $SLTO$ values; 3) the $SLTO$

parameter has no influence on R^2 for higher values of 0.1; 4) the lowest R^2 ($FKN = 0.1$ and $SLTO = 0.001$) is higher than 0.988.

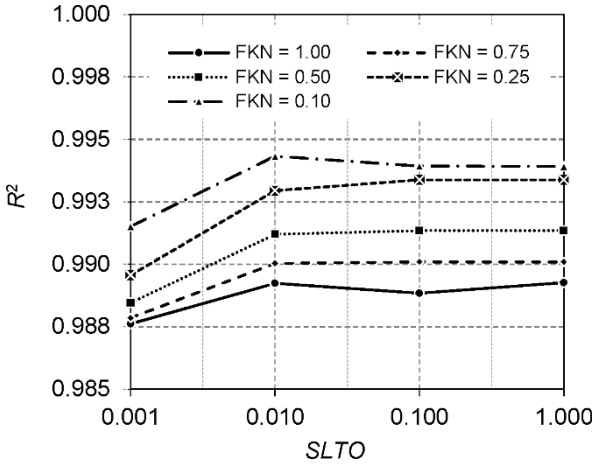

Figure 11. Values of R^2 for the different values of *SLTO* and *FKN*.

5.3. Results of the calibration model

A summary of the calibration parameters required to predict the moment-rotation curve is as follows: friction coefficient $\mu = 0.2$; fine density mesh; normal penalty stiffness factor $FKN = 0.1$; allowable elastic slip factor $SLTO = 0.01$.

Note that in all FE analysis carried out, the solutions were deemed to have converged if the square root of the sum of the squares (*SRSS*) of the residual moment imbalance was less than 0.5%.

A comparison of the moment-rotation curve from the calibrated FE model with that of Eq. (13) is given in Fig. 12. The initial rotational stiffness $\left(S_{j,ini,FEM} = 22025.369 \text{ kN/rad}\right)$ and the secant stiffness $\left(S_{j,FEM} = 7341.790 \text{ kN/rad}\right)$ of the joint are also included in Fig. 12. The intersection between the $S_{j,FEM}$ line and moment-rotation curve obtained by FEM provides the design moment resistance value $\left(M_{j,Rd,FEM} = 93.112 \text{ kNm}\right)$.

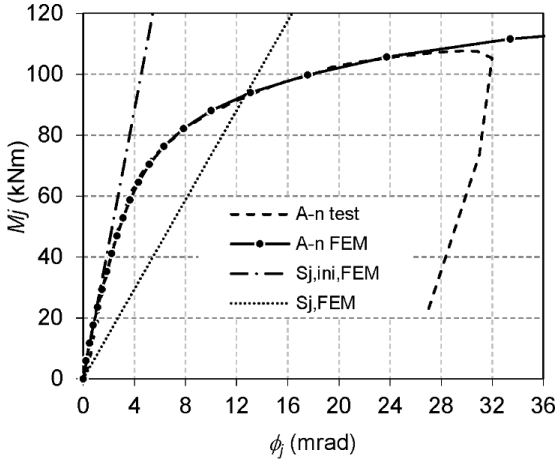

Figure 12. Calibrated moment-rotation curve of the internal joint.

The von Mises plastic strain of the internal joint is shown in Fig. 13 for the calibrated FE model where the applied moment is equal to the ultimate flexural resistance of the joint $\left(M_{j,u} = 117.344 \text{ kNm}\right)$. Strains for the tension region are greater than those for the compression region (Fig. 13a). The components which have the largest plasticity are seen to occur on the minor-axis end-plate and bolts (Fig. 13b), suggesting a mixed failure with end-plate yielding and rupture of the bolts.

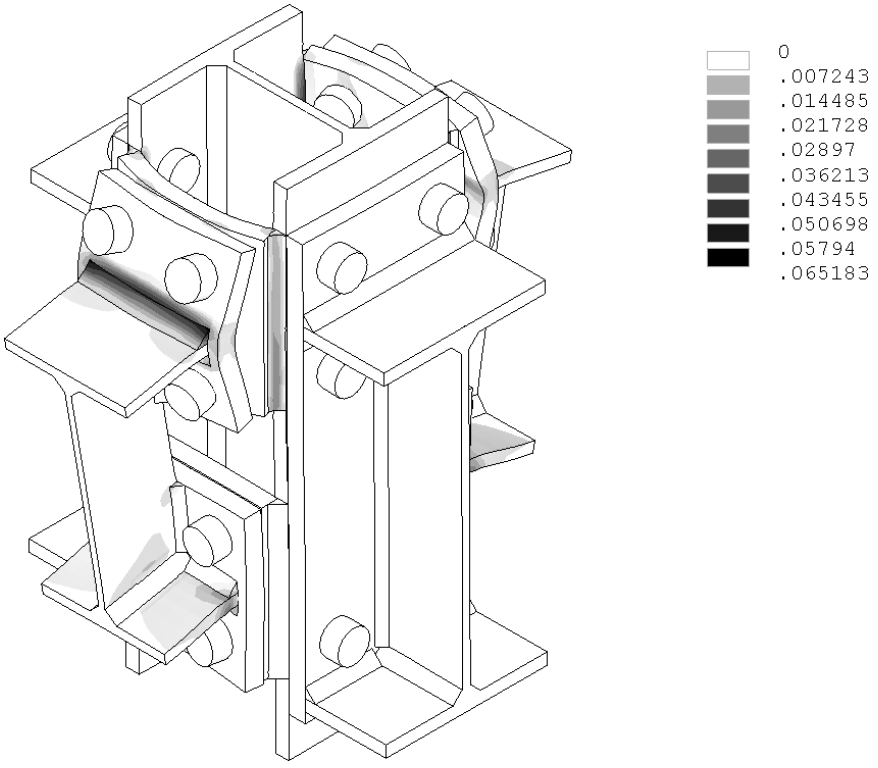

(a)

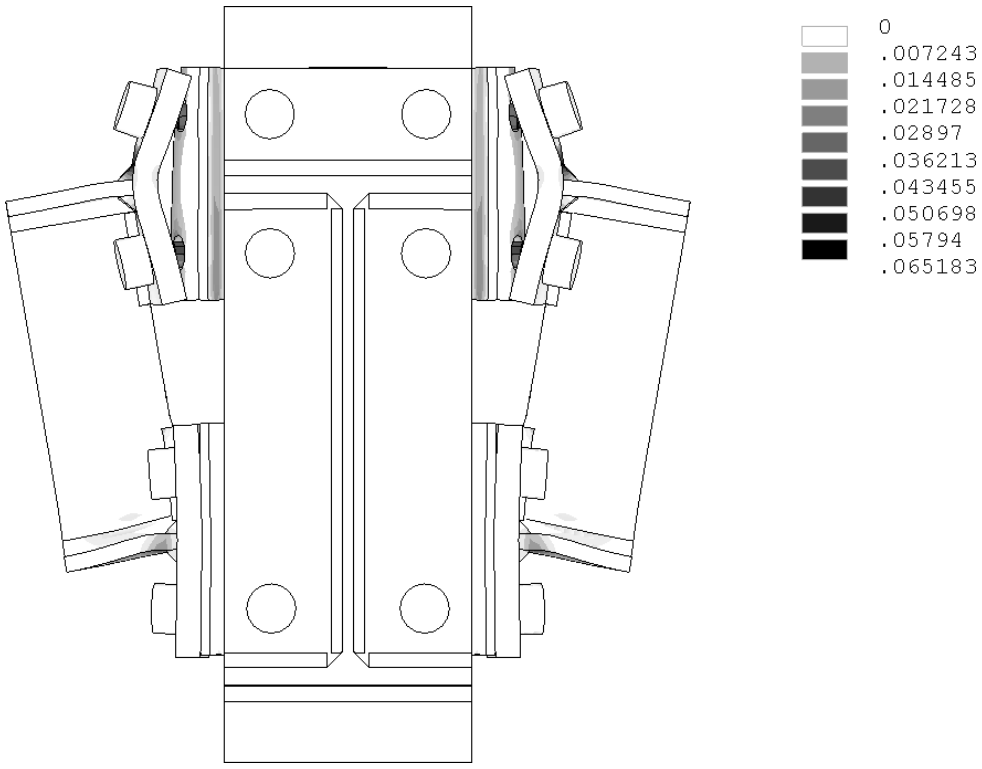

(b)

Figure 13. Von Mises plastic strain contour plot (non-plastic regions in white colour) for $M_{j,u}$=117.334 kNm (×5 amplification factor), detail of the internal joint: (a) isometric; (b) minor-axis views.

5.4 Validation of the calibrated parameters of the FE model

To validate the calibrated parameters of the FE model, these were used to analyse the internal joints of the experimental tests: A-M, B-n and B-M (Cabrero and Bayo, 2007b; Cabrero, 2006). The dimensions of the joint for the A-M, B-n, and B-M tests are given in Table 1 and the material properties are given in Table 2. Note that: 1) for the B-n and B-M tests the end-plate thickness was $t_{epM} = t_{epn} = 10$ mm ; and 2) the supporting conditions were applied at the major-axis for the A-M and B-M tests (Fig. 7a) and at the minor-axis for the B-n test (Fig. 7b).

A comparison of the moment-rotation curves produced from the FE model with the experimental tests is given in Fig. 14. The R^2 values calculated with respect to experimental results are given in Table 4, together with the sextic polynomial coefficients, Eq. (15), initial rotation stiffness and design moment resistance values.

$$p(x) = p_1 x^n + p_2 x^{n-1} + \cdots + p_n x + p_{n+1} \tag{15}$$

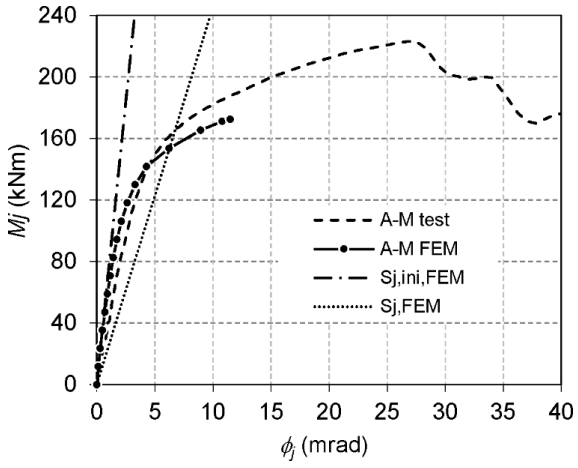

(a)

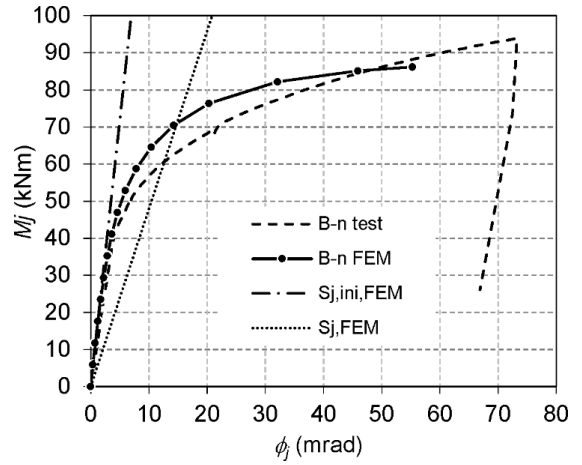

(b)

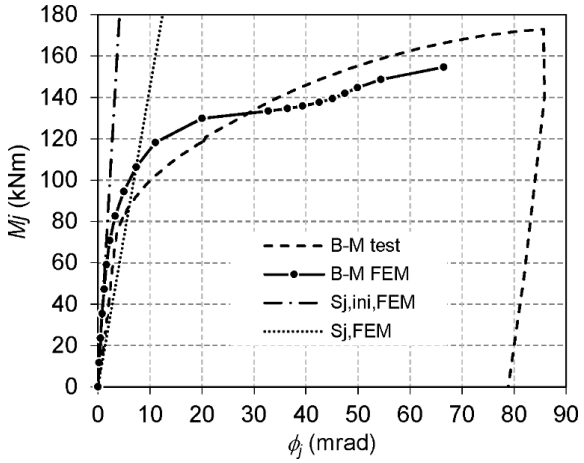

(c)

Figure 14. Validated moment-rotation curve of the joint: (a) A-M test; (b) B-n test; (c) B-M test.

Table 4. Sextic polynomial coefficients and R^2 for the moment-rotation best fit curves from the experimental results of the A-M, B-n and B-M tests (Cabrero and Bayo, 2007b).Initial rotation stiffness and design moment resistance values (kNm/rad and kNm).

Polynomial coefficients	A-M	B-n	B-M
p_1	0.000238040	-0.000000106	-0.000000585
p_2	-0.012214435	0.000021323	0.000096641
p_3	0.231090025	-0.001674438	-0.006259106
p_4	-1.838115490	0.065088934	0.201372477
p_5	3.052788025	-1.317726557	-3.370381418
p_6	38.554553185	14.089052106	29.457064698
p_7	1.011146654	-1.466881055	-3.783089165
R^2	0.913	0.963	0.915
$S_{j,ini,FEM}$	73660.675	14376.262	43467.693
$M_{j,Rd,FEM}$	153.605	70.982	106.295

The von Mises plastic strain of the joint for the A-M, B-n, and B-M tests is shown in Figs. 15, 16, and 17. Two observations can be made:

1. The FE model with the A-n calibration produces moment-rotation curve for validation tests which fit properly to the experimental curve in the elastic region, but with differences in the knee-region, Fig. 14.
2. The modes of failure suggested by the von Mises plastic strain (Figs. 15, 16 and 17) correlate with the experimental results and are:
    a. For the A-M test (Fig. 15a): the second bolt row is subjected to greater tension forces, resulting in greater elongations. The von Mises plastic strain suggests a mixed failure with plate yielding and fracture of the bolts (Fig. 15b).
    b. For the B-n test (Fig. 16a): the component which has the largest plasticity is the minor-axis end-plate. The failure (end-plate in bending) is controlled by end-plate yielding (Fig. 16b).
    c. For the B-M test (Fig. 17a): the joint behaviour is controlled (as in the B-n test) by end-plate yielding (Fig 17b).

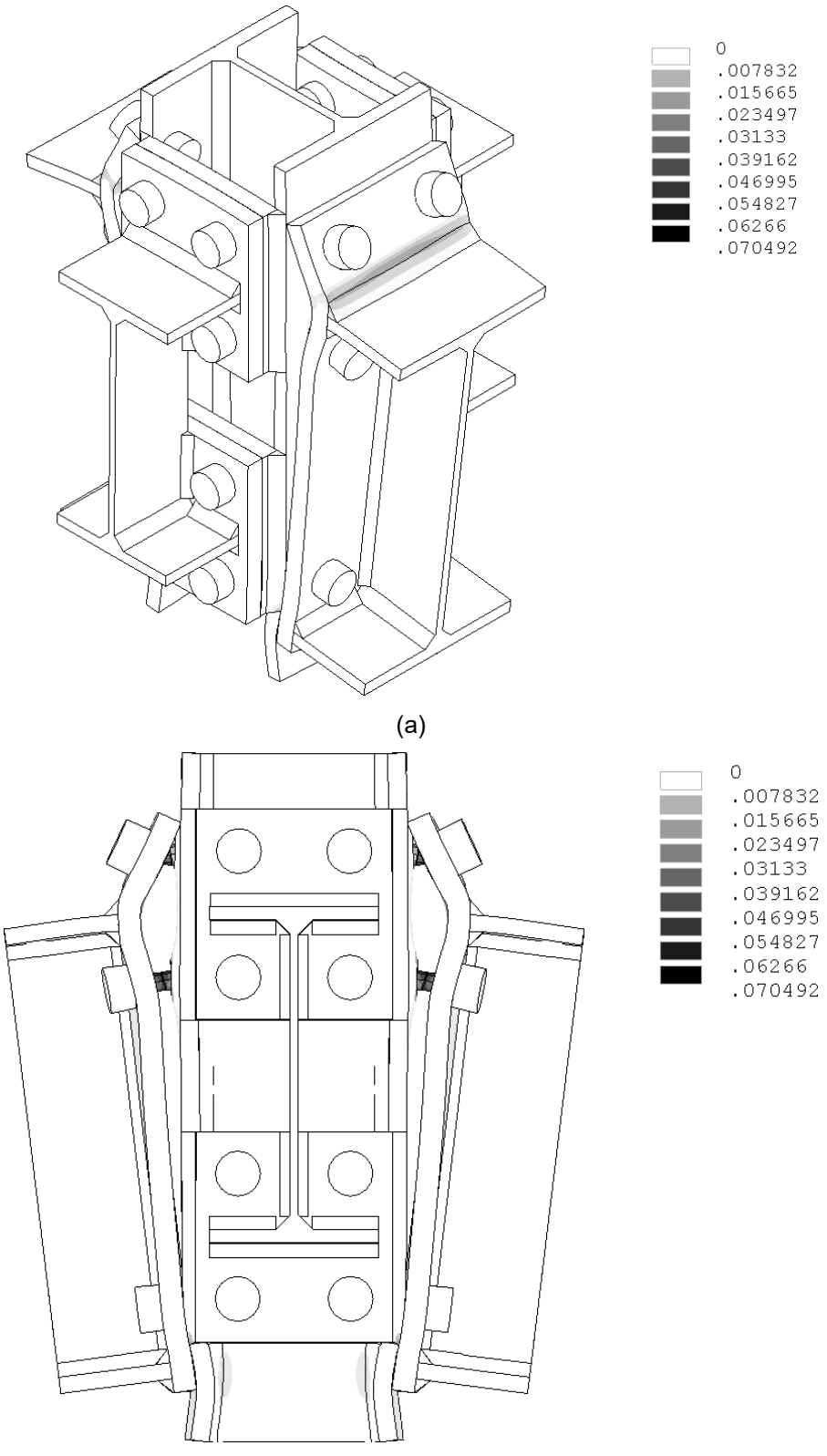

Figure 15. Von Mises plastic strain contour plot (non-plastic regions in white colour) for $M_{j,u}$ = 172.400 kNm for the A-M test (×10 amplification factor), detail of the internal joint: (a) isometric; (b) major-axis views.

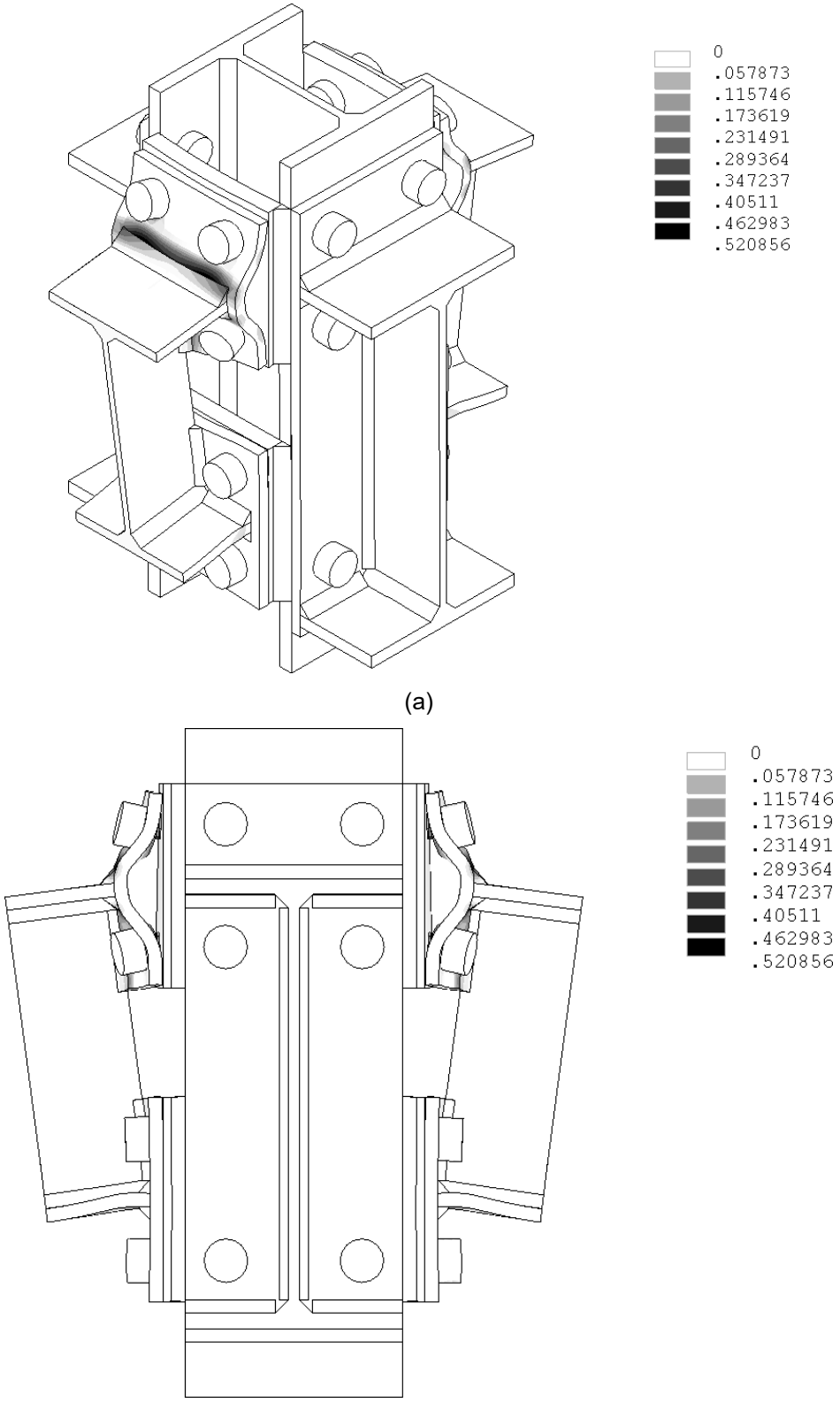

Figure 16. Von Mises plastic strain contour plot (non-plastic regions in white colour) for $M_{j,u}$ = 99.333 kNm for the B-n test (×1 amplification factor), detail of the internal joint: (a) isometric; (b) minor-axis views.

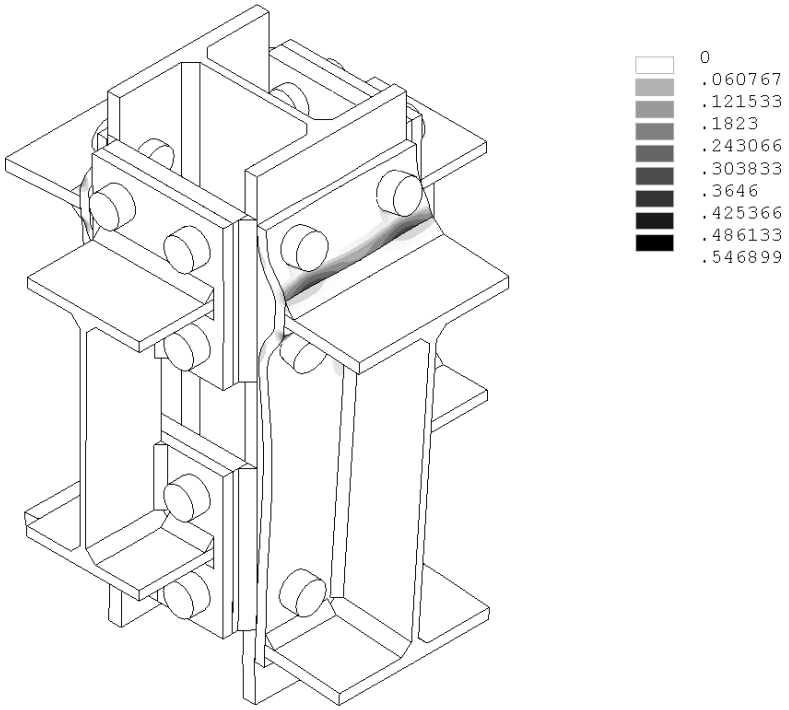

(a)

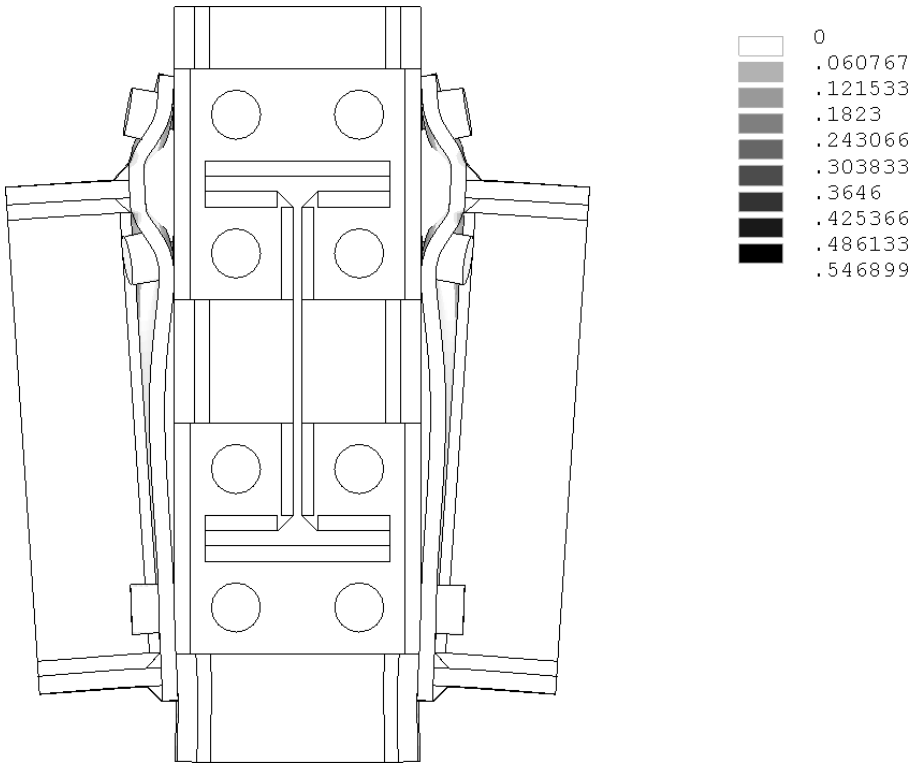

(b)

Figure 17. Von Mises plastic strain contour plot (non-plastic regions in white colour) for $M_{j,u}$=154.658 kNm for the B-M test (×1 amplification factor), detail of the internal joint: (a) isometric; (b) minor-axis views.

6. PARAMETRIC STUDIES

To demonstrate the versatility of the FE model, three parametric studies are presented which show the analysis of: 1) the effect of 3D loading with different levels of loading about minor- and major-axes on the initial stiffness of the major-axis for three joint configurations (internal, external, and corner); 2) the effect of the minor-axis beams on the major-axis rotation curve, and 3) the influence of the entire end- and additional-plates (in the minor-axis) on the major-axis joint behaviour.

A one-quarter model, using double symmetry conditions was used to generate the internal joint. For the case of the external and plane joints, a half-model using symmetry condition was used. For the corner joint, the whole model was used. To aid viewing the results, all the joints are shown as full models in the section which follow.

Type II loading and supporting conditions were used (Figs. 7c and 7d) as they allowed different load levels to be easily applied about the minor- (P_n) and the major-axes (P_M). Note that, for all parametric studies the characteristics of the FE model were those used for the A-tests.

6.1 Effect of the 3D loading

This section details the analysis of the rotational behaviour of three joint configurations: internal (IJ), external (EJ), and corner joints (CJ) (Figs. 2a, b, and c) under 3D loading. It also shows the interaction between both axes under different load levels, and its influence on the initial stiffness and the failure mode.

Although not shown here, the calibrated FE model for A-n test with type I and II boundary conditions produced the same results.

For all joint configurations, four load cases were studied:

1) Load case 1 (LC1): $P_M = P$ and $P_n = 0.00 \times P_M$

2) Load case 2 (LC2): $P_M = P$ and $P_n = 0.25 \times P_M$

3) Load case 3 (LC3): $P_M = P$ and $P_n = 0.50 \times P_M$

4) Load case 4 (LC4): $P_M = P$ and $P_n = 1.00 \times P_M$

Where the value of P value was controlled by the Newton-Raphson non-linear equation solver.

The moment-rotation curves obtained for the four 3D load cases were compared with those obtained using the analytical model provided by EC3 (EN 1993-1-8:2005, 2005). Note that the EC3 moment-rotation curve for the external, corner and plane joint configuration are the same. This is because the EC3 equations do not model the interaction of the two axes.

6.1.1 Internal joint

To obtain a 3D loading for the internal joint (Fig. 2a), four downward forces were applied on the top face of the beams: two forces (P_M) on the major-axis beams and two forces (P_n) on the minor-axis beams.

For the internal joint, a comparison was carried out of the moment-rotation curves for the major-axis produced by the FE model for different 3D load cases with that provided by the EC3 for the double-sided configuration, and is given in Fig. 18a. Three observations can be made, these are:

1. The initial stiffness value provided by the EC3 was 40000.92 kNm/rad. This value does not depend on the applied load value on the minor-axis (Fig. 18a).
2. For all load cases, the initial stiffness values obtained using the FE model (Fig. 18b) were greater than those calculated using EC3: LC1 (77117.90 kNm/rad), LC2 (83560.96 kNm/rad), LC3 (93630.32 kNm/rad), LC4 (126541.74 kNm/rad).
3. If the applied load value on the minor-axes (P_n) was increased, the major-axis initial stiffness value also increased: LC2 (8.35%), LC3 (21.41%), LC4 (64.09%) with respect to the value obtained by LC1.

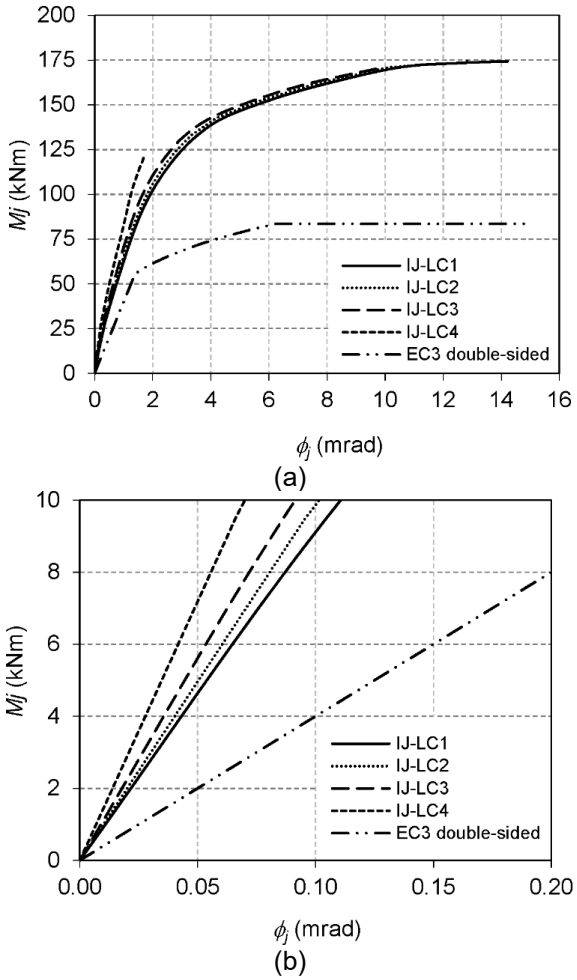

Figure 18. Major-axis moment-rotation curves for the internal joint generated from the FE model for different load cases and by EC3 for the double-sided joint configuration: (a) full curve, (b) detail of the initial region of the curve.

The von Mises plastic strain of the joint for the different load cases is shown in Fig. 19. Strains for the tension regions were greater than those in the compression regions. The components which had the largest plasticity were seen to occur on the major-axis end-plate and the bolts for the load cases 1, 2, and 3 (Figs. 19a, 19b, 19c). For load case 4 (Fig. 19d) this was seen on the minor-axis end- and additional plates and the bolts. This suggests a mixed failure, with plates yielding and with rupture of the bolts.

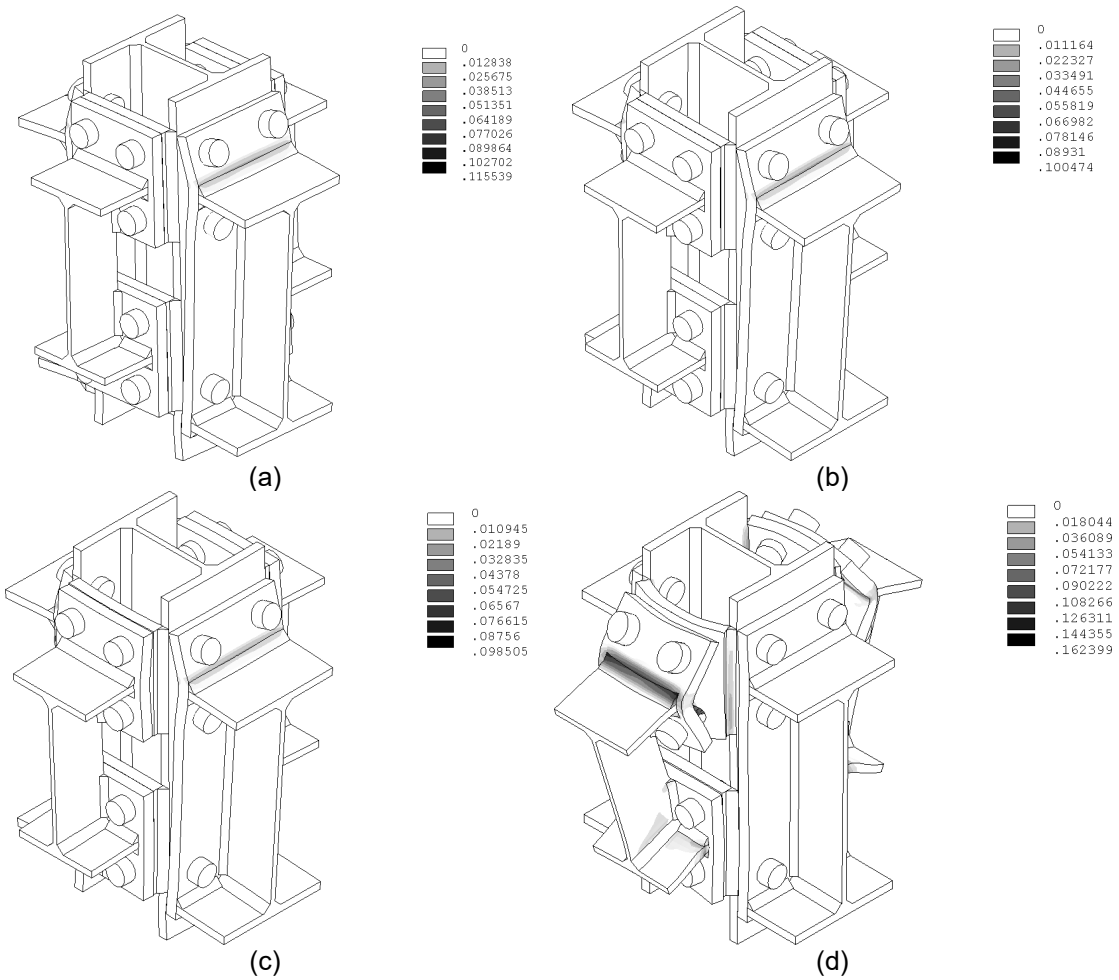

Figure 19. Von Mises plastic strain contour plot (non-plastic regions in white colour). Detail of the internal joint. Isometric view (x5 amplification factor) for: (a) LC1, (b) LC2, (c) LC3, (d) LC4.

6.1.2 External joint

To obtain a 3D loading for the external joint (Fig. 2b), three downward forces were applied on the top face of the beams: one force (P_M) on the major-axis beams and two forces (P_n) on the minor-axis beams.

For the external joint, a comparison was carried out of the moment-rotation curves for the major-axis produced by the FE model for different 3D load cases with that provided by the EC3 for the single-sided configuration, and is given in Fig. 20a. Two observations can be made, these are:

1. For all load cases, the initial stiffness values obtained using the FE model (Fig. 20b) were greater than those calculated using EC3 (20391.17 kNm/rad): LC1 (32313.99 kNm/rad; 58.47%), LC2 (33390.72 kNm/rad; 63.75%), LC3 (34732.64 kNm/rad; 70.33%), LC4 (38113.18 kNm/rad; 86.91%).
2. If the applied load value on the minor-axes (P_n) was increased, the major-axis initial stiffness value also increased: LC2 (3.33%), LC3 (7.48%), LC4 (17.95%) with respect to the value obtained by LC1.

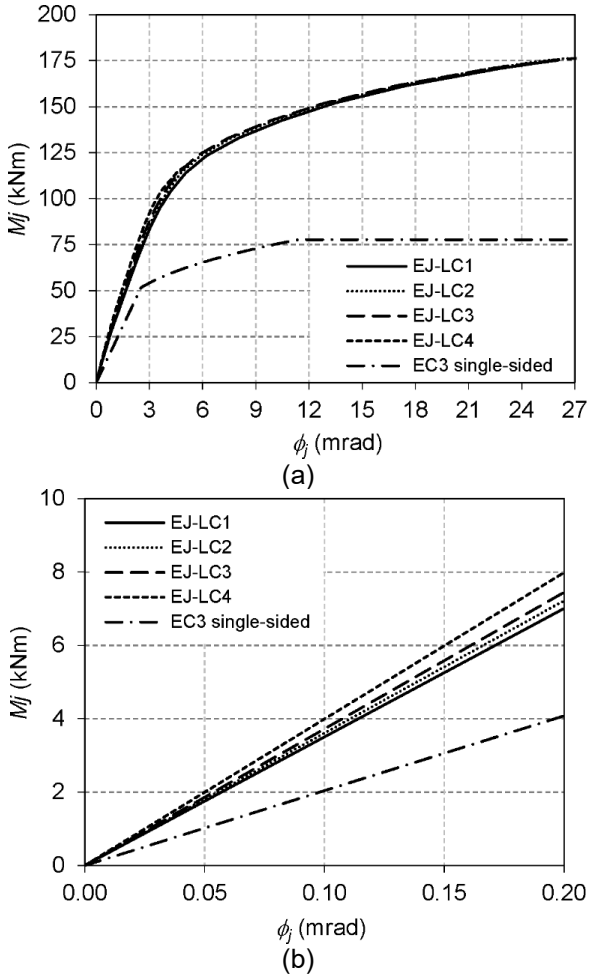

Figure 20. Major-axis moment-rotation curves for the external joint generated from the FE model for different load cases and by EC3 for the single-sided joint configuration: (a) full curve, (b) detail of the initial region of the curve.

The von Mises plastic strain of the joint for the different load cases is shown in Fig. 21. For load case 1 (Fig. 21a), 2 and 3 (not shown here) mixed failure was due to rupture of the major-axis tension bolts and yield of the compressed region of the column web.

For load case 4 (Fig. 21b), mixed failure was controlled by end- and additional- plate yielding and rupture of the minor-axis bolts.

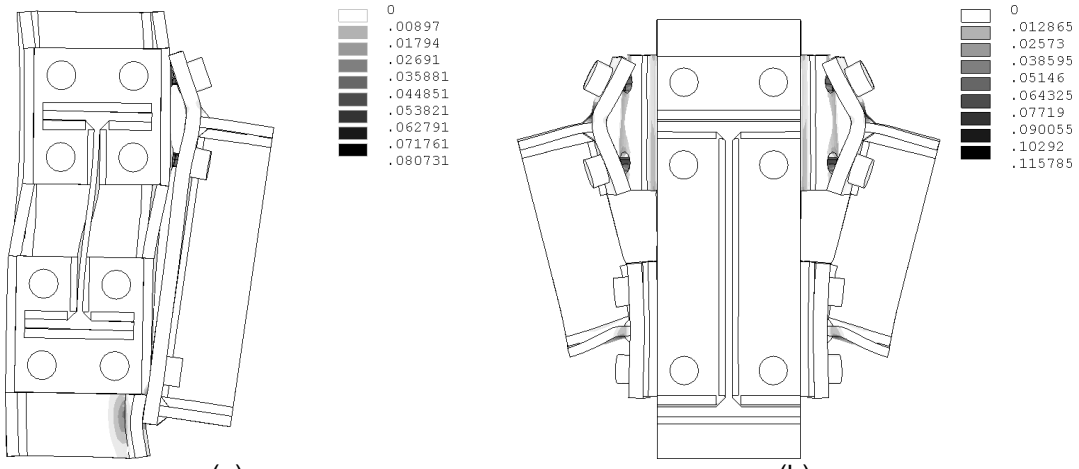

(a) (b)

Figure 21. Von Mises plastic strain contour plot (non-plastic regions in white colour). Detail of the external joint (x5 amplification factor) for: (a) LC1 (major-axis view), (b) LC4 (minor-axis view).

6.1.3 Corner joint

To obtain a 3D loading for the corner joint (Fig. 2c), two downward forces were applied on the top face of the beams: one force (P_M) on the major-axis beams and one force (P_n) on the minor-axis beams.

A comparison of the moment-rotation curves for the major-axis produced by the FE model for the different 3D load cases with that provided by the EC3 is given in Fig. 22a. Two observations can be made, these are:

1. For all the load cases studied, the initial stiffness values obtained using FE model (Fig. 22b) were greater than those calculated using EC3 (20391.17 kNm/rad): LC1 (27849.67 kNm/rad), LC2 (28112.31 kNm/rad), LC3 (28381.07 kNm/rad), LC4 (29218.38 kNm/rad).
2. If the applied load value on the minor-axis (P_n) was increased, the major-axis initial stiffness value also increased: LC2 (0.94%), LC3 (1.91%), LC4 (4.91%) with respect to the value obtained by LC1.

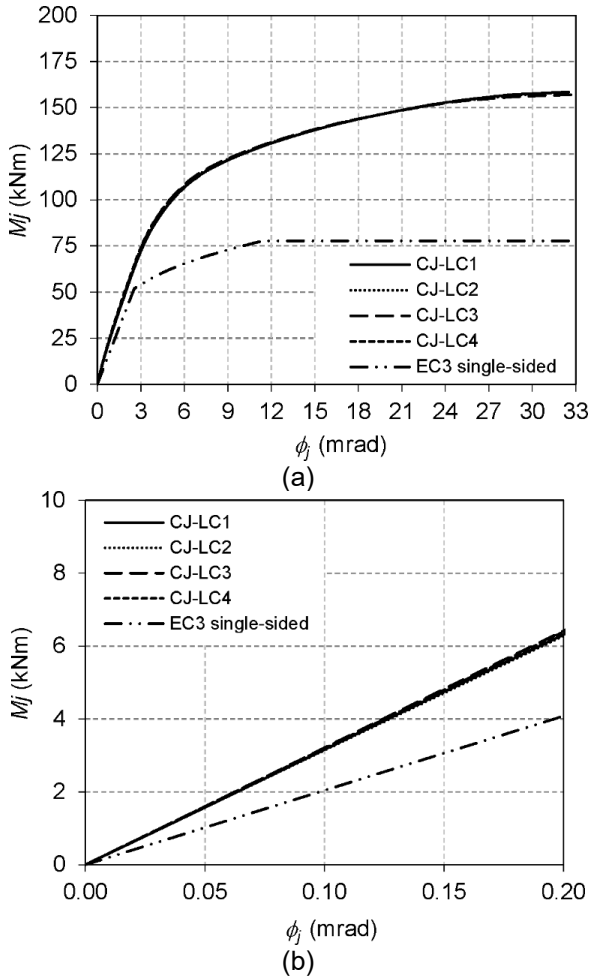

Figure 22. Major-axis moment-rotation curves for the corner joint generated from the FE model for the different load cases and by EC3 for the single-sided joint configuration: (a) full curve, (b) detail of initial region of the curve.

The modes of failure suggested by the von Mises plastic strain for load case 1 (Fig. 23a), 2 and 3 (not shown here), and 4 (Fig. 23b) correlate with those shown for the external joint configuration (Fig. 21).

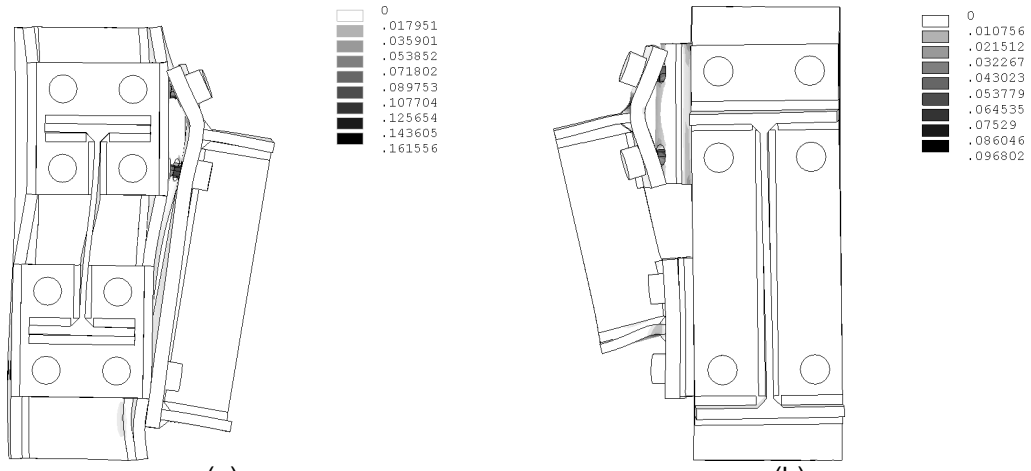

(a) (b)

Figure 23. Von Mises plastic strain contour plot (non-plastic regions in white colour). Detail of the corner joint (x5 amplification factor) for: (a) LC1 (major-axis view), (b) LC4 (minor-axis view).

6.2 Effect of the minor-axis beams on the major-axis moment-rotation curve

A parametric study was carried out on the external, corner, and plane joint configurations to determine the influence of the minor-axis beams on the major-axis moment-rotation curve. Note that, only one force (P_M) was applied on the major-axis beam.

A comparison of the moment-rotation curves for the major-axis produced by the FE model with that provided by the EC3 (for single-sided configuration) is given in Fig. 24. Three observations can be made, these are:

1. The initial stiffness value for the major-axis obtained with the FE model for the external (32313.99 kNm/rad) and the corner (27849.67 kNm/rad) joints was higher than that obtained for the plane joint (25954.55 kNm/rad).
2. For the studied joint configurations, the resulting major-axis initial stiffness values were higher than those calculated using EC3 for the single-sided configuration (20391.17 kNm/rad).
3. These results are in agreement with the idea that the EC3 underestimates the initial stiffness value by not considering the influence of the minor-axis.

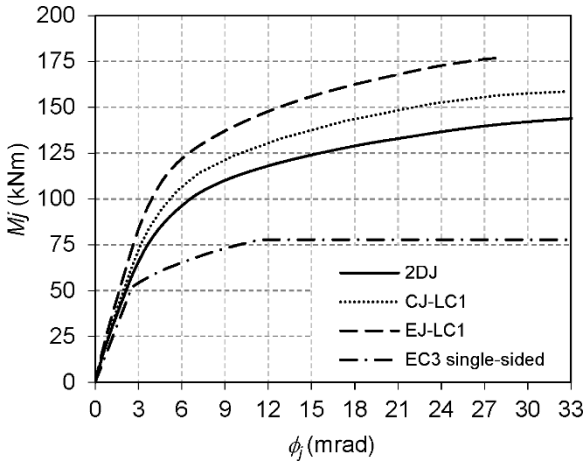

Figure 24. Major-axis moment-rotation curves generated from the FE model and EC3 for the studied joint configurations subjected to the P_M force.

6.3 Effect of the entire end- and additional-plate

An analysis was carried out of the rotational behaviour on the major-axis of the 3D joint configurations (IJ, EJ, CJ) subjected to load cases 1 and 4, when the end- and additional-plates in the minor-axis are executed as entire plates.

To obtain the FE model with the entire (full) end- and additional-plates, the clearance between the minor-axis plates value must be equal to zero $\left(H_{mid} = 0\right)$.

A comparison of the moment-rotation curves which shows the effect of the entire plates on the major-axis initial stiffness is given in Fig. 25. Two observations can be made, these are:

1. In both load cases, the effect of the entire plates is greater for the external (Fig. 25b) than for the corner joint (Fig. 25c), and is negligible for the internal joint. (Fig. 25a).
2. The use of the entire plate has an insignificant effect on the joint rotational behaviour and on its failure mode (not shown here).

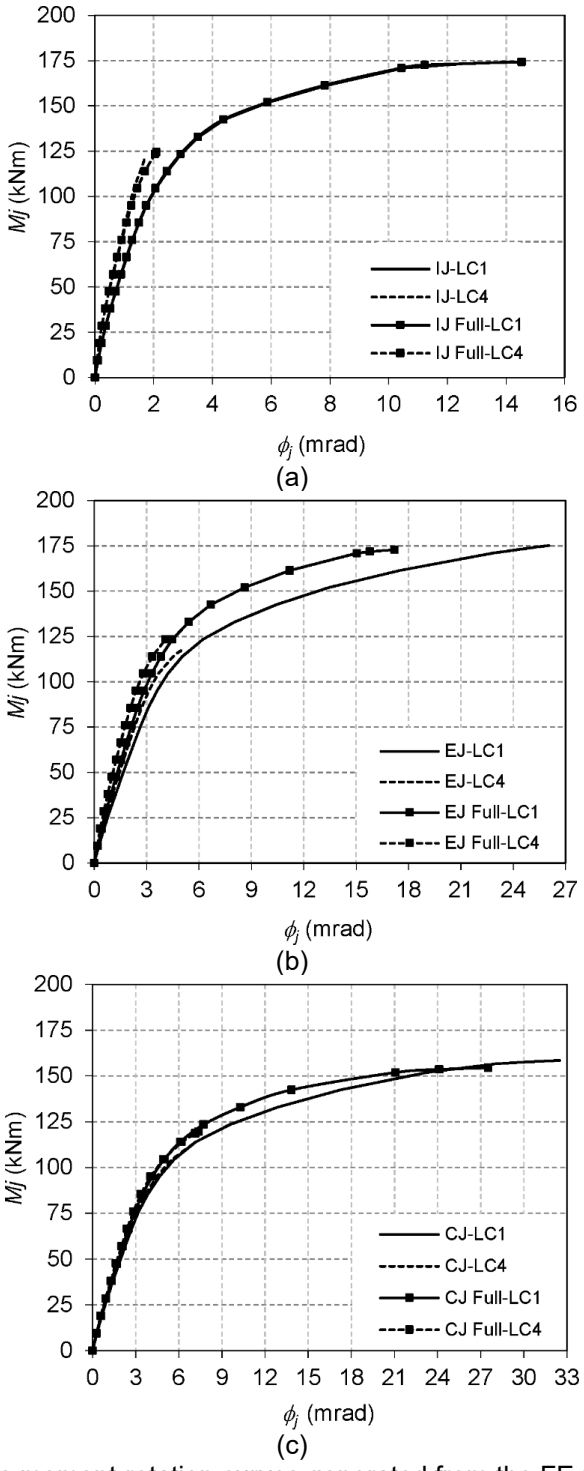

Figure 25. Major-axis moment-rotation curves generated from the FE model with the entire (full) or partial end- and additional- plates subjected to load cases 1 and 4 for: (a) internal, (b) external, (c) corner joints.

8. CONCLUSIONS

Finite element analysis is currently one of the most used methods of obtaining the mechanical behaviour of a joint. There are several reasons for this: 1) as a means of

overcoming the lack of experimental results; 2) to understand important local effects which are difficult to measure with sufficient accuracy; 3) to generate extensive parametric studies; 4) to overcome the lack of appropriate components to predict the behaviour of minor-axis and 3D joints in the current version of the component method.

This work presents a full 3D ANSYS FE parametric model to obtain the behaviour of 3D steel beam-to-column bolted extended end-plate joint in both axes. The model allows for the study of four joint configurations (internal, external, corner, and plane) and includes: contact and sliding between the different elements; bolt pre-tension; geometric and material non-linearity.

The model was calibrated and validated with the experimental moment-rotation curves of the tests A-n and A-M, B-n, and B-M (Cabrero and Bayo, 2007b). The R-square goodness-of-fit statistic was used to determine the accuracy of fit.

The validated FE model was used to study parametrically: 1) the interaction between the minor- and major- axes under 3D load cases for internal, external, and corner joint configurations; 2) the effect of the minor-axis of beams on the major-axis moment-rotation curve; and 3) the influence on the joint behaviour in the case that end- and additional-plates are executed as entire plates. The five main conclusions of these studies were:

1. A comparison of the moment-rotation curves generated from the FE model with those calculated using EC3 demonstrates that EC3 underestimates the resistance and stiffness of the joint.
2. The modes of failure suggested by the von Mises plastic strain correlate with the experimental results and EC3.
3. The initial stiffness of the major-axis increases when the applied load value on the minor-axis is increased. The other joints also experience this effect, but in a diminishing manner in the following configuration order: internal, external and corner.

4. The initial stiffness of the major-axis increases when the minor-axis beams are considered. In all studied configurations, the initial stiffness values obtained with the FE model were greater that those calculated using EC3.
5. The use of entire plates instead of partial plates in the minor-axis does not affect considerably the joint structural behaviour. The other joints also experience this effect, but in a diminishing manner in the following configuration order: external, internal and corner.

9. FINITE ELEMENT MODEL FILE

The developed ANSYS FE model can be used and downloaded for free as a single ZIP compressed file from the Technical University of Cartagena (UPCT): http://www.upct.es/goe/publicaciones/FEM_3D_EEP.zip.

For more information or questions about the FE model, please contact: Dr. Concepción Díaz Gómez (conchi.diaz@upct.es) or Dr. Osvaldo M. Querin (O.M.Querin@Leeds.ac.uk).

REFERENCES

ArcelorMittal (2016). ArcerlorMittal Europe. Long Products. “Sections and Merchant Bars”. Version: 2016-3. http://sections.arcelormittal.com/fileadmin/redaction/4-Library/1-Sales_programme_Brochures/Sales_programme/Sections_MB-ArcelorMittal_FR_EN_DE-V2016-3.pdf. Accessed 11 May 2017.

ANSYS (2016). Swanson Analysis Systems. User’s manual, version 17 and theory reference.

Augusto, H., Castro, J. M., Rebelo, C., da Silva, L. S. (2014). “A contribution to the extension of the component method to beam-to-column connections subjected to cyclic loading”, Proc. EUROSTEEL 2014, Naples, Italy.

Augusto, H., da Silva, L. S., Rebelo, C., Castro, J. M. (2016). “Characterization of web panel components in double-extended bolted end-plate steel joints”, Journal of Constructional Steel Research, 116, pp. 271-293.

Bahaari, M. R. and Sherbourne, A. N. (2000). “Behaviour of eight-bolt large capacity endplate connections”, Computers Structures, 77, pp. 315-325.

Bayo, E., Loureiro, A., Lopez, M. (2015). “Shear behaviour of trapezoidal column panels. I: Experiments and finite element modelling”, Journal of Constructional Steel Research, 108, pp. 60-69.

Bose, S. K., McNeice, G. M., Sherbourne, A. N. (1972). “Column webs in steel beam to column connexions. Part I: formulation and verification”, Computers Structures, 2, pp. 253-72.

Bursi, O. S. and Jaspart, J. P. (1997a). “Benchmarks for finite element 50nions50s50 of bolted steel connections”, Journal of Constructional Steel Research, 43, pp. 17-42.

Bursi, O. S. and Jaspart, J. P. (1997b). “Calibration of a finite element model for isolated bolted end plate steel connections”, Journal of Constructional Steel Research, 44(3), pp. 225-262.

Bursi, O. S. and Jaspart, J. P. (1998). “Basic issues in the finite element simulation of extended end plate connections”, Computer Structures, 69, pp. 361-382.

Cabrero, J. M. (2006). Nuevas propuestas para el diseño de 50nions50s y 50nions semirrígidas de acero. Ph. Thesis (in Spanish). Spain. University of Navarra.

Cabrero, J. M. and Bayo, E. (2007a). “The semi-rigid behaviour of three-dimensional steel beam-to-column steel joints subjected to proportional loading. Part II: Theoretical model and validation”, Journal of Constructional Steel Research, 63, pp. 1254-1267.

Cabrero, J. M. and Bayo, E. (2007b). “The semi-rigid behaviour of three-dimensional steel beam-to-column steel joints subjected to proportional loading. Part I: Experimental evaluation”, Journal of Constructional Steel Research, 63, pp. 1241-1253.

Dabaon, M. A., El-Boghdadi, M. H., Kharoob, O. F. (2009). “Experimental and numerical model for space steel and composite semi-rigid joints”, Journal of Constructional Steel Research, 65, pp. 1864-1875.

Dai, X. H., Wang, Y. C., Bailey, C. G. (2010). “Numerical modelling of structural fire behaviour of restrained steel beam-column assemblies using typical joint types”, Engineering Structures, 32: pp. 2337-2351.

Díaz, C. (2010). Optimum design of semi-rigid joint by numeric simulation and kriging models. Ph.D. Thesis (in Spanish; ISBN: 978-1-124-341606). Spain. Technical University of Cartagena.

Díaz, C., Victoria, M., Martí, P., Querin, O. M. (2011). “FE model of beam-to-column extended end-plate joints”, Journal of Constructional Steel Research, 67, pp. 1578-1590.

EN 14399-3:2005 (2005). European Committee for Standardisation (CEN). “High-strength structural bolting assemblies for preloading. Part 3: System HR-Hexagon bolt and nut assemblies”. Brussels.

EN 1993-1-1:2005 (2005). European Committee for Standardisation (CEN). Eurocode 3. Design of steel structures, part 1-1: General rules and rules for buildings. Brussels.

EN 1993-1-8:2005 (2005). European Committee for Standardisation (CEN). Eurocode 3. Design of steel structures, part 1-8: design of joints. Brussels.

Faella, C., Piluso, V., Rizzano, G. (2000). Structural steel semirigid connections: theory, design and software. New directions in civil engineering. Boca Raton, Florida: CRC publishers; (EEUU).

Gan, S., Xuesen, Ch., Dongyang, W. (2017). “Experimental study of ultra-large capacity end-plate joints”, Journal of Constructional Steel Research, 128, pp. 354-361.

Gil, B. and Bayo, E. (2008). “An alternative design for internal and external semi-rigid composite joints. Part II: Finite element modelling and analytical study”, Engineering Structures, 30, pp. 232-246.

Gil, B., Goñi, R., Bayo, E. (2013). “Experimental and numerical validation of a new design for three-dimensional semi-rigid composite joints”, Engineering Structures, 48, pp. 55-69.

Jordão, S., Simões da Silva, L., Simões, R. (2013). “Behaviour of welded beam-to-column joints with beams of unequal depth”, Journal of Constructional Steel Research, 91, pp. 42-59.

Loureiro, A., López, M., Gutiérrez, R., Reinosa, J. M. (2013a). “Experimental and numerical analysis of E-stubs in three dimensional joints: A new analytical formulation for the stiffness calculation”, Engineering Structures, 53, pp. 1-9.

Loureiro, A., López, M., Gutiérrez, R., Reinosa, J. M. (2013b). “A new analytical formulation for the E-stub strength calculation in three dimensional steel joints with additional plates welded to the weak axis”, Engineering Structures, 56, pp. 2263-2272.

Loureiro, A., Moreno, A., Gutiérrez, R., Reinosa, J. M. (2012). “Experimental and numerical analysis of three-dimensional semi-rigid steel joints under non-proportional loading”, Engineering Structures, 38, pp. 68-77.

Maggi, Y. I., Gonçalves, R. M., Leon, R. T., Ribeiro, L. F. L. (2005). “Parametric analysis of steel bolted end plate connections using finite element modelling”, Journal of Constructional Steel Research, 61, pp. 689-708.

MATLAB R2016a (2016). MathWorks, Inc. Natick, MA.

Sherbourne, A. N. and Bahaari, M. R. (1996). “3D simulation of end-plate bolted connections”, Journal of Structural Engineering, 120(11), pp. 3122-3136.

Tagawa, H. and Gurel, S. (2005). “Application of steel channels as stiffeners in bolted moment connections”, Journal of Constructional Steel Research, 61(12), pp. 1650-1671.